


Article

Electrochemically Induced Cu-NiOOH/Cu₂O/Cu Mesh Heteroarchitecture with Cu-Ni Dual Active Sites as Efficient Bifunctional Electrocatalyst for Urea-Assisted Energy-Saving Hydrogen Production in Alkaline Electrolyte

Kaige Zhao [†], Xinhao Xu [†], Manli Wang, Tao Chen, Qianlin Ju, Lulu Hao, Zelin Chen ^{*} , Xiaolong Yu ^{*} and Changjiu Li ^{*}

State Key Laboratory of Marine Resource Utilization in South China Sea, School of Materials Science and Engineering, Hainan University, Haikou 570228, China; zhaokaige@hainanu.edu.cn (K.Z.); 20213006771@hainanu.edu.cn (X.X.); manliwang33@163.com (M.W.); chent@hainanu.edu.cn (T.C.); 21220856000029@hainanu.edu.cn (Q.J.); 23210805000003@hainanu.edu.cn (L.H.)

^{*} Correspondence: zelinchen@hainanu.edu.cn (Z.C.); yuxiaolong@hainanu.edu.cn (X.Y.); lichangjiu@hainanu.edu.cn (C.L.)

[†] These authors contributed equally to this work.



Citation: Zhao, K.; Xu, X.; Wang, M.; Chen, T.; Ju, Q.; Hao, L.; Chen, Z.; Yu, X.; Li, C. Electrochemically Induced Cu-NiOOH/Cu₂O/Cu Mesh Heteroarchitecture with Cu-Ni Dual Active Sites as Efficient Bifunctional Electrocatalyst for Urea-Assisted Energy-Saving Hydrogen Production in Alkaline Electrolyte. *Catalysts* **2024**, *14*, 496. <https://doi.org/10.3390/catal14080496>

Academic Editor: Justo Lobato

Received: 30 June 2024

Revised: 16 July 2024

Accepted: 20 July 2024

Published: 1 August 2024



Copyright: © 2024 by the authors. Licensee MDPI, Basel, Switzerland. This article is an open access article distributed under the terms and conditions of the Creative Commons Attribution (CC BY) license (<https://creativecommons.org/licenses/by/4.0/>).

Abstract: The electrocatalytic oxidation of urea combined with wastewater splitting is considered a promising approach for sustainable hydrogen production, characterized by minimal energy consumption. However, its evolution is greatly hindered by the shortage of efficient and easily accessible electrocatalytic materials. Here, a facile electrochemical activation strategy was conceived and proposed to construct a Cu-doped NiOOH nanolayer encapsulated on Cu₂O nanodendrites on Cu mesh substrate (Cu-NiOOH/Cu₂O/CM) from the electrodeposited Ni/Cu₂O/CM heterostructured precatalyst. It was verified that the incorporation of Cu not only facilitates the rapid formation of Ni^(III) species but also contributes to the formation of Cu-Ni^(III) bifunctional electrocatalytic active sites. Benefiting from the accessible Cu-Ni^(III) dual active sites, high active surface area, good hydrophilic and aerophobic surface properties and superior electrical conductivity of the Cu mesh substrate, the as-prepared Cu-NiOOH/Cu₂O/CM exhibits enhanced bifunctional electrocatalytic abilities for electrocatalytic urea oxidation reaction (UOR) and hydrogen evolution reaction (HER). Particularly, for the Cu-NiOOH/Cu₂O/CM || Cu-NiOOH/Cu₂O/CM configuration toward the UOR || HER coupled system, a significantly reduced cell voltage of 1.43 V vs. RHE @ 10 mA·cm⁻² was obtained. The observed cell voltage for the conventional overall water splitting is approximately 190 mV higher than that observed for overall urea splitting. This study proposes a viable approach to achieve and optimize the bifunctional UOR/HER performance of NiOOH active species, which holds significant importance for efficient and stable hydrogen generation from urea-contaminated substandard water.

Keywords: Cu; NiOOH; electrochemical activation; urea oxidation reaction; hydrogen evolution reaction; electrocatalysis

1. Introduction

Recent studies have shown that electrochemically converting urea, originating from biological urine and industrial effluents, into sustainable green hydrogen is a potential solution to effectively address eutrophication caused by urea pollution in water bodies and energy shortages [1–3]. The UOR, with a thermodynamic potential of 0.37 V, exhibits a significantly lower energy requirement compared to the oxygen evolution reaction (OER), which necessitates 1.23 V [4]. This leads to the suggestion of adopting UOR in place of OER as the anodic oxidation reaction in water electrolysis can notably elevate hydrogen production efficiency [5]. Nevertheless, the efficiency of urea electrolysis is impeded by the sluggish kinetics of anodic UOR and cathodic HER in alkaline media [6]. The UOR

process, which involves a six-electron transfer mechanism ($\text{CO}(\text{NH}_2)_2 + 6\text{OH}^- \rightarrow \text{N}_2 + \text{CO}_2 + 5\text{H}_2\text{O} + 6\text{e}^-$), necessitates the meticulous design of highly efficient electrocatalysts with rational nanostructures and compositions, as well as possessing bifunctional electrocatalytic properties for both UOR and HER.

Throughout the last few decades, electrocatalysts based on noble metals (Pt, Pd, Ir, and Ru) have been extensively employed in water electrolysis for hydrogen production, owing to their excellent electrocatalytic activities for UOR, OER, and HER [7–9]. Despite this, the scarcity, high cost, and mono-functional nature of noble metals sharply curtail their broad application [10,11]. Therefore, the exploration of high-performance non-metallic bifunctional catalysts for overall urea splitting is crucial in replacing noble metal-based alternatives, enabling efficient and energy-efficient hydrogen production from wastewater containing urea [12]. Previous investigations have demonstrated that Ni-based catalysts possess significant potential as practical bifunctional electrocatalysts for UOR and HER [13–15]. The presence of eight electrons in the 3D orbital endows Ni with its exceptional electrocatalytic properties. In an alkaline electrolyte, the UOR mechanism involving Ni^{II} active sites invariably leads to self-oxidation, resulting in the formation of trivalent Ni^{III} species on the surface (typically at ~ 1.36 V) [4]. These species serve as the veritable active sites for UOR. The potential reaction pathway is $6\text{NiOOH} + \text{CO}(\text{NH}_2)_2 + 6\text{OH}^- \rightarrow 6\text{Ni}(\text{OH})_2 + \text{N}_2 + \text{CO}_2 + 5\text{H}_2\text{O} + 6\text{e}^-$.

Nevertheless, the direct synthesis of NiOOH electrocatalysts results in relatively low electrical conductivity, potentially limiting their catalytic performance and making it difficult to achieve bifunctional catalytic properties [16,17]. Therefore, various nickel-based compound nanomaterials with different morphologies, structures, and crystalline forms, such as Ni_2S_3 [18,19], Ni_3S_4 [20,21], NiTe [22], and NiSe [23,24] catalysts, have been designed and synthesized. These materials demonstrate variable valence states on their surface component and rapid in situ electrochemical reconstruction during the electrocatalytic process [25]. For instance, Tu et al. [26] applied an activation technique to change the original nickel foam into a fluffy nanosheet structure (I-NiS). In an alkaline electrolyte, the I-NiS electrode exhibited exceptional UOR performance, achieving a 100 mA cm^{-2} current density at only 1.44 V vs. RHE. The NiOOH species formed during the catalytic process were verified in the veritable catalytic active site according to the in situ Raman spectroscopy characterization. Yang et al. [27] presented a synthetic approach for fabricating ultra-thin 2D nanomaterial $\text{Ni}(\text{OH})_2$, and the investigation unveiled that the edges of $\text{Ni}(\text{OH})_2$ exhibit enhanced reactivity in generating NiOOH species and adsorbing urea molecules compared to the basal plane, thereby accelerating the catalytic kinetics of UOR. It exhibits strong catalytic activity in electrochemical tests, and its activity increased by 5.7 times at a potential relative to Ag/AgCl of 0.6 V. Nonetheless, the design of such Ni-based electrocatalysts was intricate, the synthesis procedures were relatively complex, and the NiOOH species formed via electrochemical activation still function as single catalytic active sites in the reaction.

In view of the aforementioned challenges, here, we report a Cu-NiOOH/ Cu_2O /CM heterostructured nanocatalyst with Cu- Ni^{III} dual active sites, which was obtained via a facile electrochemical activation treatment of the electrodeposited Ni/ Cu_2O /CM precatalyst. Structural characterization combined with surface valence state analysis demonstrates that the NiOOH species formed during electrochemical activation feature an amorphous structure. Additionally, the electronic structure of Cu on the surface was also modified due to the generation of Ni^{III} , yielding highly intrinsically active Cu- Ni^{III} dual active sites. According to electrochemical characterization, to obtain the UOR current densities of 10 mA cm^{-2} and 100 mA cm^{-2} , the Cu-NiOOH/ Cu_2O /CM catalyst requires the potentials of only 1.32 V and 1.38 V vs. RHE, respectively. Furthermore, the Cu-NiOOH/ Cu_2O /CM catalyst shows a Pt-like HER activity in a urea-rich electrolyte, requiring the overpotentials of 71 mV and 196 mV to attain the HER current densities of 10 mA cm^{-2} and 100 mA cm^{-2} , respectively. The application of the Cu-NiOOH/ Cu_2O /CM || Cu-NiOOH/ Cu_2O /CM configuration in a two-electrode electrolyzer was also investigated, highlighting excel-

lent activity and durability for overall urea electrolysis. Overall, the as-prepared Cu-NiOOH/Cu₂O/CM catalyst exhibits excellent UOR/HER bifunctional electrocatalytic activity and durability, ascribed to the well-defined architecture of the Cu₂O nanodendrites, and most importantly, the high intrinsic activity of the Cu-Ni^(III) dual active sites.

2. Results and Discussion

Figure 1a depicts the preparation pathway employed for the Cu-NiOOH/Cu₂O/CM catalyst. Initially, a facile corrosion and oxidation approach was utilized to enable the in situ growth of abundant branched nanostructures composed of Cu(OH)₂ and Cu₂O adorned on the surface of Cu mesh (referred to as Cu(OH)₂/CM and Cu₂O/CM). Subsequently, Ni nanoparticles were deposited onto the surface of Cu₂O/CM through an electrochemical reduction strategy in a nickel-containing electrolyte, resulting in the formation of the heterostructural Ni/Cu₂O/CM catalyst. By adjusting the electrodeposition time (120, 240, and 360 s), the Ni loading on the Cu₂O nanodendrites surface was conveniently controlled, with the morphologies of the samples presented in Figure S3. It was observed that the amount of Ni particles deposited increased rapidly with prolonged deposition time. The sample with 240 s of electrodeposition demonstrated the most uniform deposition of Ni nanoparticles. However, after 360 s of electrodeposition, there was substantial agglomeration of Ni particles on the Cu₂O nanodendrites surface, which would evidently impact the subsequent electrochemical activation process. Consequently, the sample with 240 s of electrodeposition was chosen for subsequent electrochemical activation treatment as the Ni/Cu₂O/CM precatalyst. Ultimately, through a straightforward electrochemical activation step (see Section 3 and Figure S2 for details), the Cu-NiOOH/Cu₂O/CM heteroarchitectures were successfully synthesized. Correspondingly, the surface morphologies of the pristine CM, Cu(OH)₂/CM, Cu₂O/CM, Ni/Cu₂O/CM, and Cu-NiOOH/Cu₂O/CM electrodes are displayed in Figure 1b,k and Figure S4. The process of Cu(OH)₂ converting to Cu₂O was validated by XRD characterization, as demonstrated in Figure S5. Evidently, the porous structure of the Cu mesh substrate remains consistent during the preparation process, whereas well-defined nanodendrites, about 100 nm in diameter, uniformly grow on the Cu mesh surface, becoming progressively rougher and denser. According to previous studies, nanodendrites exhibit an expanded electrochemical active surface area (ECSA), enhanced active site efficiency, and accelerated mass and charge transfer, highlighting the suitability of Cu-NiOOH/Cu₂O/CM catalyst for electrocatalysis in UOR and HER [28–30]. According to the Brunauer–Emmett–Teller (BET) surface area analysis (Figure S6), the surface areas of the pristine CM, Cu(OH)₂/CM, Cu₂O/CM, Ni/Cu₂O/CM, and Cu-NiOOH/Cu₂O/CM samples are measured to be 12.79, 13.88, 15.09, 20.60, and 13.49 cm²·mg^{−1}, respectively. This observation reveals that the deposition of Ni nanostructures onto the Cu₂O surface enhances the surface area, while the subsequent electrochemical activation slightly reduces the surface area of Cu-NiOOH/Cu₂O/CM. Subsequent electrochemical performance tests have confirmed the improved UOR and HER activity of Cu-NiOOH/Cu₂O/CM, indirectly highlighting the enhanced intrinsic activity of the Cu-NiOOH dual active sites [31,32].

To elucidate the intricate morphology and structural composition of the Ni/Cu₂O/CM pre-catalyst and Cu-NiOOH/Cu₂O/CM catalysts, Transmission electron microscopy (TEM) and corresponding selected-area electron diffraction (SAED) techniques were employed. As illustrated in Figure 1c, the Ni nanoparticles are visibly clear and evenly distributed on the surface of Cu₂O nanorods, averaging a particle size of approximately 20.67 nm (Figure S7). The high-resolution TEM (HRTEM) image depicted in Figure 1d confirms that Ni nanoparticles are decorated on both the surface and internal sections of Cu₂O nanorods in the Ni/Cu₂O/CM sample, revealing distinct lattice fringes with interplanar distances of around 0.207 nm and 0.214 nm, which can be attributed to the Ni(111) and Cu₂O(200) planes [33]. In the SAED image (Figure 1e), several bright spots can be observed forming concentric rings, which indicate the polycrystalline nature of the Ni/Cu₂O/CM, with three types of diffraction rings corresponding to Ni, Cu₂O, and Cu species. The corresponding high-angle annular dark-field (HAADF) image accompanied by element

mapping images (Figure 1f–j) demonstrates that the nanorods comprise Ni, Cu, and O elements, with Ni elements conspicuously distributed on the periphery of Cu, in agreement with the TEM findings.

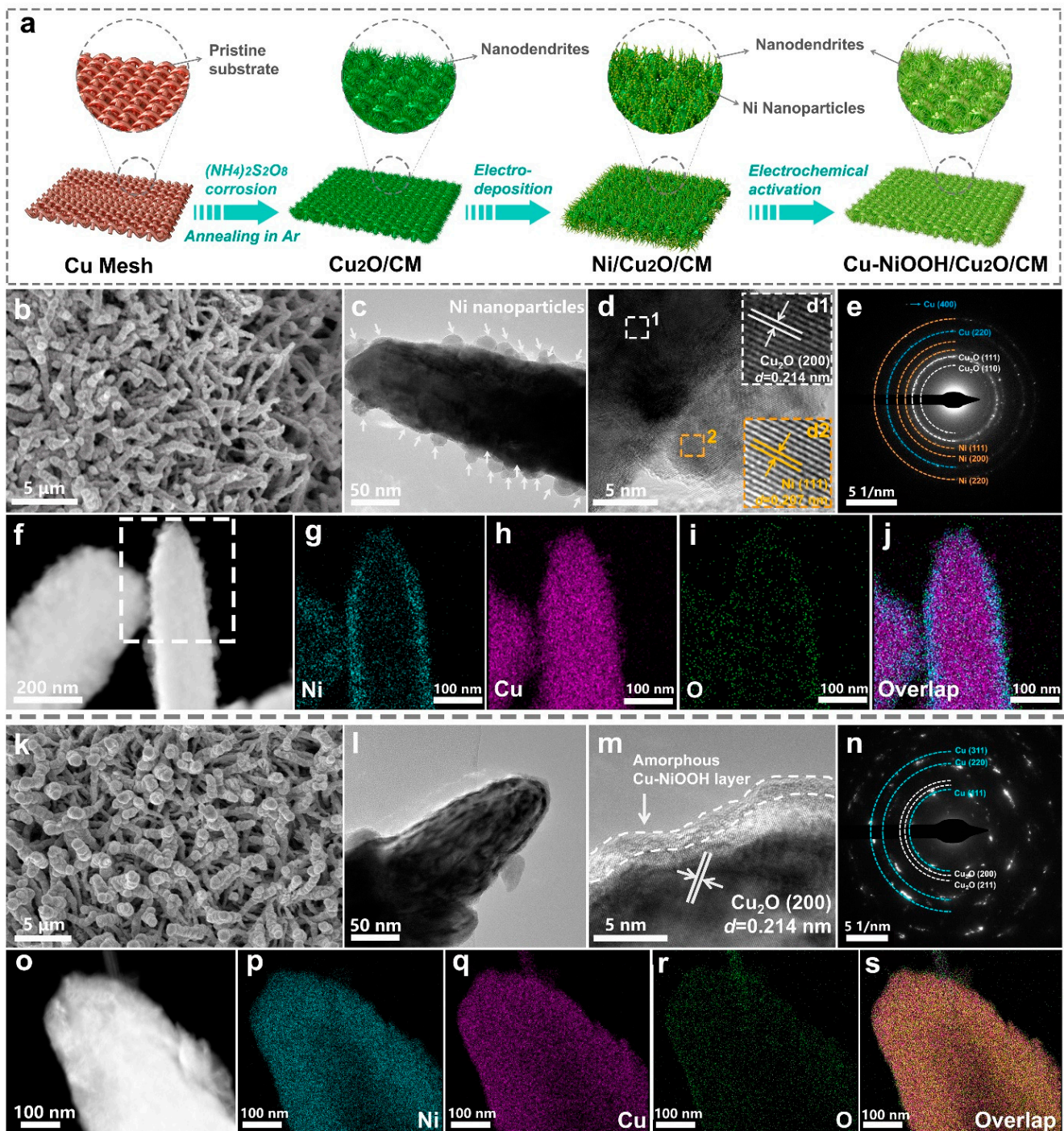


Figure 1. Synthesis, structure and morphology characterizations of Ni/Cu₂O/CM and Cu-NiOOH/Cu₂O/CM catalysts. (a) Schematic illustration of the synthesis process. (b,k) SEM images of Ni/Cu₂O/CM and NiOOH/Cu₂O/CM catalysts; (c,l) low-resolution TEM (The arrows indicate the locations where Ni nanoparticles are deposited) and (d,m) HRTEM images of Ni/Cu₂O/CM and NiOOH/Cu₂O/CM catalysts; (e,n) corresponding SAED pattern, (f,o) HAADF-STEM images and (g–j,p–s) EDS elemental mapping of Ni/Cu₂O/CM and NiOOH/Cu₂O/CM catalysts within the corresponding dashed box regions, respectively.

Moreover, for the Cu-NiOOH/Cu₂O/CM catalyst obtained by electrochemical activation, the TEM image depicted in Figure 1l reveals that the surface Ni nanoparticles have disappeared substantially post-activation, with a thin, low-crystallinity layer forming on the nanodendrites. The HRTEM characterization (Figure 1m) results demonstrate that the low-crystallinity species in the outer layer have a thickness of about 1–2 nm, potentially indicating a NiOOH layer, which requires further characterization to confirm. The lattice spacing of the internal Cu₂O remains unchanged at 0.214 nm, consistent with the results shown in Figure 1d. The SAED image (Figure 1n) demonstrates that the Cu-NiOOH/Cu₂O/CM sample exhibits diffraction rings solely corresponding to Cu and Cu₂O, and no diffraction rings associated with NiOOH species were observed, suggesting the NiOOH layer formed possesses low crystallinity, which is in accordance with the HRTEM results. The associated HAADF image combined with the element mapping images (Figure 1o–s) indicates that after electrochemical activation treatment, Cu distributes within the surface range of Ni, accompanied by a concentration of O on the surface, suggesting that Cu has been incorporated into the NiOOH layer. On the whole, the successful fabrication of Cu-NiOOH/Cu₂O heteroarchitectures on CM substrate is strongly supported by all these remarkable results.

X-ray diffraction (XRD) was also carried out to assess the crystalline phase of pristine CM, Cu(OH)₂/CM, Cu₂O/CM, Ni/Cu₂O/CM, and Cu-NiOOH/Cu₂O/CM samples, and the results are illustrated in Figure 2a. For the Cu-NiOOH/Cu₂O/CM sample, the diffraction peaks located at $2\theta = 36.4^\circ$, 42.3° , 50.5° , 61.4° and 73.6° were discerned, indexing to the (111), (200), (211), (220) and (310) planes of Cu₂O (JCPDS card No. 65-3288), respectively [34]. As presented in the enlarged XRD pattern of Cu-NiOOH/Cu₂O/CM depicted in Figure S8, the diffraction peaks, positioned at $2\theta = 42.1^\circ$ and 43.4° , were observed to overlap with the diffraction peaks of Cu₂O and Cu, which can be attributed to the (111) and (210) crystallographic planes of NiOOH (JCPDS card No. 27-0956) [35]. Therefore, supplementary characterization is essential to confirm the occurrence of NiOOH species in the Cu-NiOOH/Cu₂O/CM material. Other three pronounced diffraction peaks centered at $2\theta = 43.3^\circ$, 50.7° and 74.2° were observed as well, which can be attributed to the (111), (200) and (220) planes of the Cu mesh substrate (JCPDS card No. 04-0836) [36]. Moreover, the as-prepared Ni/Cu₂O/CM, and Cu₂O/CM materials also exhibited similar XRD patterns. Specifically, there is no distinct diffraction peak attributed to Ni species except for a weaker diffraction peak centered at $2\theta = 44.9^\circ$ observed in the Ni/Cu₂O/CM sample, which may be attributed to either a low Ni content or the poor crystallinity.

To further investigate the structural transformation of Ni and Cu species during the electrochemical activation process, Raman spectroscopy was performed at room temperature on Cu₂O/CM, Ni/Cu₂O/CM, and Cu-NiOOH/Cu₂O/CM samples in the range of 100–900 cm^{−1}, as illustrated in Figure 2b. As shown, the Cu₂O and CuO species exhibited characteristic Raman bands at 148, 217, 280 and 631 cm^{−1} and in 324 cm^{−1}, respectively, in the Cu₂O/CM catalyst. After the electrochemical activation process, the similar-looking Raman spectra can be observed in Ni/Cu₂O/CM sample [37]. Moreover, the electrodeposited Ni nanoparticles in Ni/Cu₂O/CM exhibited no distinguishable characteristics, indicating the absence of any Raman allowed bands in metallic Ni, which is in agreement with the HRTEM observations (Figure 1c,d). Specially, the Cu-NiOOH/Cu₂O/CM sample showed a broad peak centered at approximately 522 cm^{−1}, which could be attributed to Ni–O and Cu–O bands, indicating the formation of Cu-NiOOH [38].

X-ray photoelectron spectroscopy (XPS) analysis was executed to capture the surface elemental compositions and valence states of the as-synthesized Ni/Cu₂O/CM pre-catalyst and Cu-NiOOH/Cu₂O/CM catalyst. Figure S9 shows that the survey XPS spectra of Ni/Cu₂O/CM and Cu-NiOOH/Cu₂O/CM samples reflect the presence of Cu, Ni, and O elements, in line with the EDS mapping results. Figure 2c shows the Ni 2p XPS spectra for Cu-NiOOH/Cu₂O/CM, Ni/Cu₂O/CM samples and pristine Ni mesh for comparison. As displayed, two additional sharp peaks at 857.2 and 876.1 eV can be observed in the Ni 2p_{3/2} and Ni 2p_{1/2} high-resolution spectrum of the Cu-NiOOH/Cu₂O/CM catalyst, which can

only be attributed to the trivalent Ni^{3+} sites formed throughout the electrochemical activation procedure [39]. For comparison, the spectrum of $\text{Ni } 2p_{3/2}$ in the $\text{Ni}/\text{Cu}_2\text{O}/\text{CM}$ sample and the spectrum of $\text{Ni } 2p_{3/2}$ and $\text{Ni } 2p_{1/2}$ in the Ni mesh sample displayed less pronounced peaks associated with zero-valent Ni^0 , demonstrating that the electrodeposited Ni nanoparticles were in the metallic state, in agreement with the HRTEM observations (Figure 1c,d). The vanishing of zero-valent Ni^0 in the $\text{Cu-NiOOH}/\text{Cu}_2\text{O}/\text{CM}$ sample results from the thorough oxidation of Ni species during the electrochemical activation phase (Figure S2). Furthermore, a considerable amount of divalent Ni^{2+} was also detected in all samples. The oxidation of Ni in the air, which is inevitable, can be attributed to this phenomenon [40]. Additionally, the $\text{Cu } 2p$ XPS spectra for the $\text{Cu-NiOOH}/\text{Cu}_2\text{O}/\text{CM}$ and $\text{Ni}/\text{Cu}_2\text{O}/\text{CM}$ samples are presented in Figure 2d. The $\text{Cu}_2\text{O}/\text{CM}$ sample was also investigated for comparative purposes. As illustrated, the high-resolution $\text{Cu } 2p_{3/2}$ and $2p_{1/2}$ spectrum for $\text{Cu}_2\text{O}/\text{CM}$ shows two major peaks at binding energies of 932.4 eV and 952.2 eV, associated with Cu^+ species, along with minor peaks at 934.6 eV and 954.6 eV, corresponding to Cu^{2+} species [41]. A strong electronic interaction between the surface-deposited Ni species and Cu_2O can be inferred from the 1.3 eV shift to higher binding energies of the $\text{Cu}^+ 2p_{3/2}$ and $2p_{1/2}$ peaks upon Ni surface electrodeposition [42]. Additionally, compared to the $\text{Ni}/\text{Cu}_2\text{O}/\text{CM}$ samples, the $\text{Cu}^+ 2p$ peaks in the $\text{Cu-NiOOH}/\text{Cu}_2\text{O}/\text{CM}$ samples shift by 0.3 eV towards lower binding energies, suggesting that during the electrochemical activation process, the Cu sites on the material's surface acquire partial electrons, facilitating the formation of $\text{Ni}^{(\text{III})}$ [31]. Similar phenomena have been observed in recent research. For instance, Luo and colleagues [43] demonstrated that the introduction of Cu heteroatoms not only promotes the formation of Ni^{3+} in the $\text{Ni}_2\text{P-Ni}_{12}\text{P}_5$ heterojunction but also accelerates electron transfer between Cu and NiOOH , thereby exhibiting enhanced performance for UOR.

To accurately disclose the contribution of Cu incorporation into NiOOH sites to improving OER performance, CV measurements were employed and conducted in a three-electrode cell system with a 1.0 M KOH electrolyte at room temperature, and the half-cycle CV curves from the negative potential sweep were depicted in Figure S10a. The pristine CM , $\text{Cu}(\text{OH})_2/\text{CM}$, $\text{Cu}_2\text{O}/\text{CM}$ and IrO_2 catalysts were also examined for comparison. As shown, a relatively higher OER activity is exhibited by the $\text{Cu-NiOOH}/\text{Cu}_2\text{O}/\text{CM}$ catalyst among these catalysts. To reach a HER current density of $10 \text{ mA}\cdot\text{cm}^{-2}$, the $\text{Cu-NiOOH}/\text{Cu}_2\text{O}/\text{CM}$ catalyst requires an overpotential of 290 mV, which is more advantageous than those of IrO_2 (330 mV), $\text{Cu}_2\text{O}/\text{CM}$ (420 mV), $\text{Cu}(\text{OH})_2/\text{CM}$ (470 mV), and pristine CM (530 mV) samples (Figure S10c). Moreover, Tafel plots were applied to evaluate the OER electrocatalytic reaction kinetics for each catalyst. As illustrated in Figure S10b, the $\text{Cu-NiOOH}/\text{Cu}_2\text{O}/\text{CM}$ catalyst demonstrated a relatively lower Tafel slope of $44.9 \text{ mV}\cdot\text{dec}^{-1}$, in comparison with those of IrO_2 ($67.9 \text{ mV}\cdot\text{dec}^{-1}$), $\text{Cu}_2\text{O}/\text{CM}$ ($78.5 \text{ mV}\cdot\text{dec}^{-1}$), $\text{Cu}(\text{OH})_2/\text{CM}$ ($143.0 \text{ mV}\cdot\text{dec}^{-1}$), and pristine CM ($165.0 \text{ mV}\cdot\text{dec}^{-1}$) samples, revealing the enhanced OER kinetics on $\text{Cu-NiOOH}/\text{Cu}_2\text{O}/\text{CM}$ with Cu-NiOOH dual active sites.

The Nyquist plots in Figure S10d were obtained from EIS characterization and fitted with the appropriate equivalent circuit, with R_s signifying the electrolyte resistance and R_{ct} signifying the charge transfer resistance at the electrode-electrolyte interface [44,45]. As illustrated, the $\text{NiOOH}/\text{Cu}_2\text{O}/\text{CM}$ catalyst demonstrates lower R_s (1.30Ω) and R_{ct} (2.83Ω) values relative to other as-prepared catalysts, indicating a higher charge transfer rate during the OER process, which is likely caused by the synergistic effect between the $\text{Ni}^{(\text{III})}$ active sites and the doping of Cu in $\text{Cu-NiOOH}/\text{Cu}_2\text{O}/\text{CM}$ catalyst. Additionally, the calculation of the double-layer capacitance (C_{dl}) from CV curves was utilized to determine the electrochemically active surface area (ECSA) of different $\text{Cu-NiOOH}/\text{Cu}_2\text{O}/\text{CM}$, $\text{Cu}_2\text{O}/\text{CM}$ and $\text{Cu}(\text{OH})_2/\text{CM}$ electrodes, as depicted in Figure S10e. It should be highlighted that the $\text{Cu-NiOOH}/\text{Cu}_2\text{O}/\text{CM}$ catalyst has a noteworthy calculated C_{dl} value of $20.3 \text{ mF}\cdot\text{cm}^{-2}$, smaller than those of $\text{Cu}_2\text{O}/\text{CM}$ ($31.7 \text{ mF}\cdot\text{cm}^{-2}$) and $\text{Cu}(\text{OH})_2/\text{CM}$ ($58.9 \text{ mF}\cdot\text{cm}^{-2}$). This implies that the ECSA of the $\text{Cu-NiOOH}/\text{Cu}_2\text{O}/\text{CM}$ catalyst has unexpectedly decreased

after electrochemical activation. Considering the improved OER performance, one can infer that the intrinsic activity of the Cu-NiOOH dual active sites in Cu-NiOOH/Cu₂O/CM is much higher than that of the single Cu active site in Cu₂O/CM and Cu(OH)₂/CM catalysts. Comparable results were also observed in preceding studies [46]. Furthermore, the assessment of long-term durability toward OER was conducted through chronopotentiometry measurement, as depicted in Figure S10f. It is worth mentioning that the Cu-NiOOH/Cu₂O/CM catalyst sustained a stable overpotential at OER current densities of 10 and 100 mA·cm⁻² over a 16 h test period, and the CV curves displayed negligible variation before and after the long-term chronopotentiometry test.

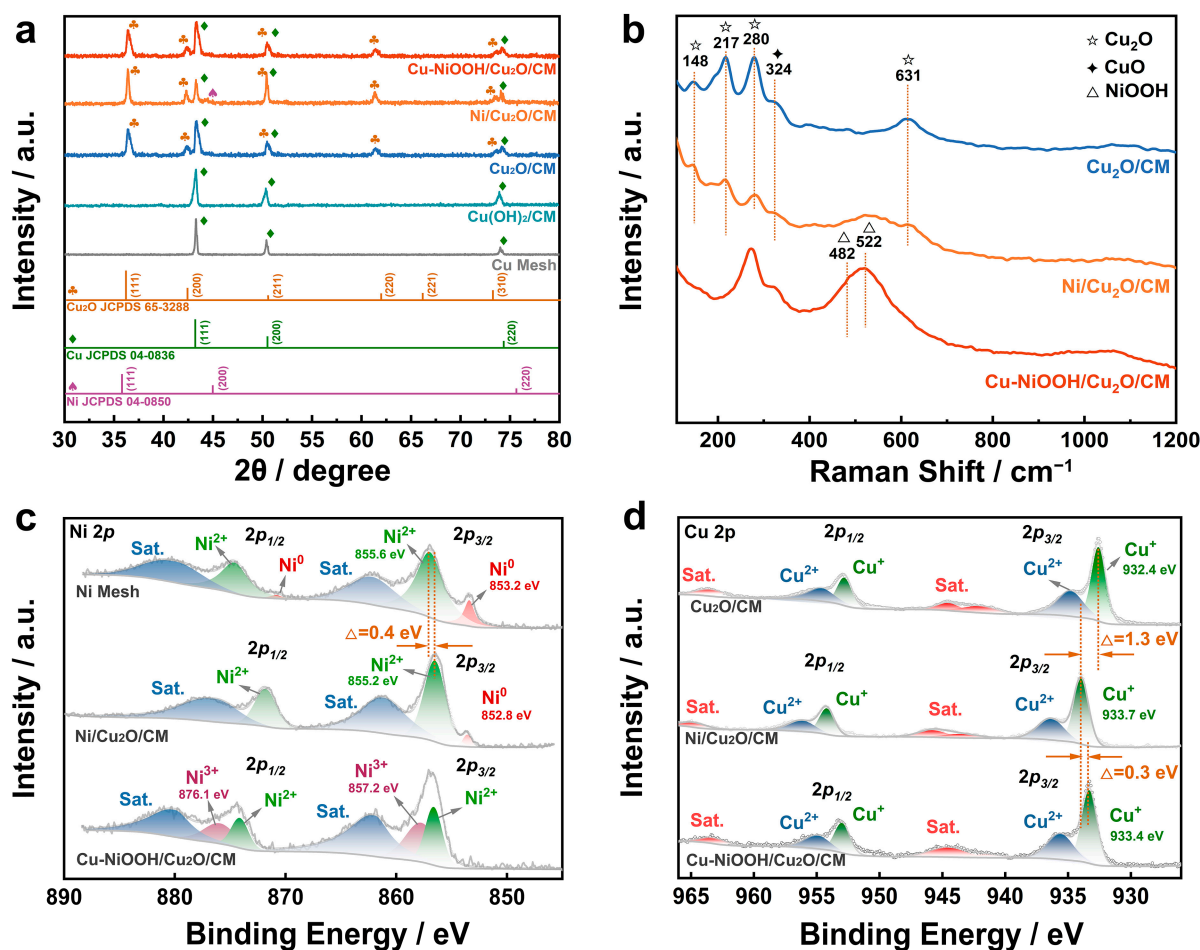


Figure 2. (a) XRD patterns of CM, Cu(OH)₂/CM, Cu₂O/CM, Ni/Cu₂O/CM, and Cu-NiOOH/Cu₂O/CM. (b) Raman spectra; high-resolution XPS of (c) Ni 2p in Ni Mesh, Ni/Cu₂O/CM and Cu-NiOOH/Cu₂O/CM samples, respectively, and (d) Cu 2p in Cu₂O/CM, Ni/Cu₂O/CM and Cu-NiOOH/Cu₂O/CM samples, respectively.

The UOR electrocatalytic activities of the Cu-NiOOH/Cu₂O/CM sample were primarily evaluated in a 1.0 M KOH solution with and without 0.5 M urea. According to Figure 3a, the potentials needed for the Cu-NiOOH/Cu₂O/CM catalyst to attain current densities of 10 and 100 mA·cm⁻² in UOR are 1.32 and 1.38 V vs. RHE, respectively, which are much lower compared to those for OER (1.53 and 1.62 V vs. RHE to achieve current densities of 10 and 100 mA·cm⁻², respectively). The observed reduction in potential underscores the thermodynamic advantages of UOR over OER, and implies that utilizing UOR instead of anodic OER can facilitate energy-efficient hydrogen generation at lower potentials [47]. For comparison, the UOR performance of the as-prepared pristine CM, Cu(OH)₂/CM, Cu₂O/CM, IrO₂, and Cu-NiOOH/Cu₂O/CM samples was also determined in a 1.0 M KOH with 0.5 M urea electrolyte and the UOR curves are displayed in Figure 3b. As shown,

Cu-NiOOH/Cu₂O/CM requires the lowest potential to deliver 10 and 100 mA·cm⁻² (Figure 3c) compared to that of IrO₂ (1.37 and 1.48 V vs. RHE), Cu₂O/CM (1.50 and 1.69 V vs. RHE), Cu(OH)₂/CM (1.45 and 1.73 V vs. RHE) and pristine CM (1.50 and 1.90 V vs. RHE). The UOR activity of Cu-NiOOH/Cu₂O/CM is also higher than that of the majority of catalysts reported in recent publications (as shown in Figure 3g and Table S1), indicating that Cu-NiOOH/Cu₂O/CM catalysts with Cu-NiOOH dual-active sites induced by an electrochemical activation process exhibit high-efficiency catalysis of urea decomposition. To uncover the UOR dynamics on different catalysts, the corresponding Tafel slopes were plotted in Figure 3d. As shown, the as-synthesized Cu-NiOOH/Cu₂O/CM catalyst exhibits a relatively minimal Tafel slope of 17 mV·dec⁻¹, significantly smaller than that of IrO₂ (34 mV·dec⁻¹), Cu₂O/CM (102 mV·dec⁻¹), Cu(OH)₂/CM (117 mV·dec⁻¹), and pristine CM (171 mV·dec⁻¹). The observed smallest Tafel slope from Cu-NiOOH/Cu₂O/CM indicates its accelerated UOR reaction kinetics, which is likely caused by the synergistic effect between the Ni^(III) active sites and the doping of Cu in Cu-NiOOH/Cu₂O/CM catalyst and the unique electronic configuration among the components (Figure 3c,d) [48]. As exhibited in Figure S11, the determined C_{dl} values of the as-synthesized Cu-NiOOH/Cu₂O/CM, Cu₂O/CM and Cu(OH)₂/CM catalysts were 17.2, 37.3 and 48.2 mF·cm⁻², suggesting that the electrochemically activated Cu-NiOOH/Cu₂O/CM catalyst possesses a relatively lower ECSA value. This also indicates that the intrinsic activity of the Cu-NiOOH dual active sites in Cu-NiOOH/Cu₂O/CM substantially exceeds that of the single Cu active site in Cu₂O/CM and Cu(OH)₂/CM catalysts toward UOR [49]. Moreover, to further probe the electron-transfer kinetics, an EIS analysis was also conducted and the spectra were recorded at 1.40 V vs. RHE. The Nyquist plots illustrated that the Cu-NiOOH/Cu₂O/CM sample exhibited an R_s value of 1.30 Ω and a smaller R_{ct} value of 0.90 Ω (Figure 3e) compared with that of IrO₂ (R_s = 1.60 Ω, R_{ct} = 2.70 Ω), Cu₂O/CM (R_s = 1.50 Ω, R_{ct} = 5.45 Ω), Cu(OH)₂/CM (R_s = 1.50 Ω, R_{ct} = 8.16 Ω) and pristine CM (R_s = 1.80 Ω, R_{ct} = 9.25 Ω) electrode, indicating a higher charge transfer rate during the UOR process for Cu-NiOOH dual active sites in Cu-NiOOH/Cu₂O/CM. Furthermore, chronopotentiometry was employed to assess the long-term durability of UOR, as elaborated in Figure 3f. It was observed that the Cu-NiOOH/Cu₂O/CM catalyst sustained a stable overpotential at UOR current densities of 10 and 100 mA·cm⁻² over a 16 h test period, and the CV curves displayed negligible variation before and after the long-term chronopotentiometry test.

To uncover the bifunctional catalytic characteristics of the Cu-NiOOH/Cu₂O/CM catalyst in urea-containing water, CVs were primarily performed in a 1.0 M KOH electrolyte both with and without the presence of 0.5 M urea. As presented in Figure 4a, the HER activity of Cu-NiOOH/Cu₂O/CM catalyst was similar regardless of the urea presence in the electrolyte, implying that the HER efficiency is well preserved during urea-containing wastewater treatment [50]. For comparison, the HER activities of the as-prepared Cu-NiOOH/Cu₂O/CM, Ni/Cu₂O/CM, Cu₂O/CM, Cu(OH)₂/CM, pristine CM samples and the commercial Pt/C were also determined in a 1.0 M KOH with 0.5 M urea electrolyte and the HER polarization curves are displayed in Figure 4b. As shown, Cu-NiOOH/Cu₂O/CM requires a Pt-like overpotential of 71 and 196 mV to deliver the HER current density of 10 and 100 mA·cm⁻² in urea-rich electrolyte (1.0 M KOH + 0.5 M urea), respectively, smaller compared to that of Ni/Cu₂O/CM (210 and 450 mV), Cu₂O/CM (392 and 565 mV), Cu(OH)₂/CM (431 and 613 mV) and pristine CM (486 and 781 mV) (Figure 4c). Among recently reported catalysts, the HER activity of the electrochemically activated Cu-NiOOH/Cu₂O/CM catalyst is notably higher (Figure 4g and Table S2), highlighting the HER electrocatalytic potential of the Cu-NiOOH dual active sites. To uncover the HER dynamics on different catalysts, the corresponding Tafel slopes were plotted in Figure 4d. As shown, the as-synthesized Cu-NiOOH/Cu₂O/CM catalyst exhibits a relatively minimal Tafel slope of 73 mV·dec⁻¹, slightly lower than that of Pt/C (54 mV·dec⁻¹) but significantly smaller than that of Ni/Cu₂O/CM (126 mV·dec⁻¹), Cu₂O/CM (211 mV·dec⁻¹), Cu(OH)₂/CM (216 mV·dec⁻¹), and pristine CM (233 mV·dec⁻¹). As presented in Figure 4e, the Nyquist plots illustrated that the Cu-NiOOH/Cu₂O/CM sample exhibited a R_s value of

1.20 Ω and a smaller R_{ct} value of 4.20 Ω , compared with that of Ni/Cu₂O/CM ($R_s = 1.30 \Omega$, $R_{ct} = 8.25 \Omega$), Cu₂O/CM ($R_s = 1.30 \Omega$, $R_{ct} = 9.37 \Omega$), Cu(OH)₂/CM ($R_s = 1.30 \Omega$, $R_{ct} = 13.56 \Omega$) and pristine CM ($R_s = 1.20 \Omega$, $R_{ct} = 23.54 \Omega$) electrode, indicating a higher charge transfer rate during the HER process for Cu-NiOOH dual active sites in Cu-NiOOH/Cu₂O/CM. Furthermore, Figure 4f depicts the long-term HER chronopotentiometry testing in a 1.0 M KOH + 0.5 M urea electrolyte for the Cu-NiOOH/Cu₂O/CM catalyst. It was observed that the Cu-NiOOH/Cu₂O/CM catalyst sustained a stable overpotential at HER current densities of 10 mA·cm⁻² over a 16 h test period, and the CV curves displayed negligible variation before and after the long-term chronopotentiometry test in a 1.0 M KOH + 0.5 M urea electrolyte.

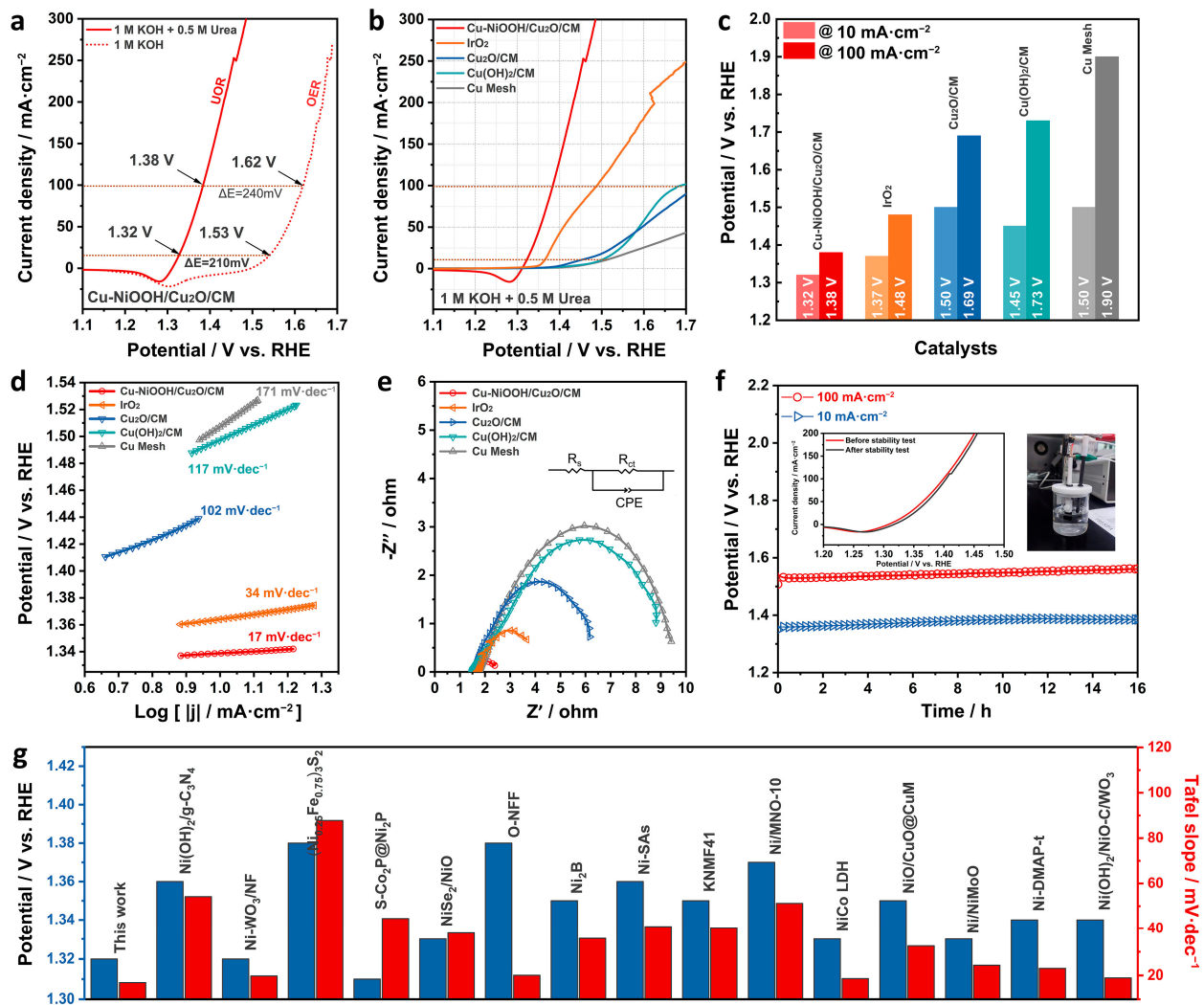


Figure 3. Electrocatalytic UOR properties. (a) Polarization curves of Cu-NiOOH/Cu₂O/CM catalyst in a 1.0 M KOH electrolyte with and without 0.5 M urea. (b) Polarization curves of Cu-NiOOH/Cu₂O/CM, IrO₂, Cu₂O/CM, Cu(OH)₂/CM and pristine CM. (c) Summarized potential at the UOR current density of 10 and 100 mA·cm⁻². (d) Tafel slopes. (e) Nyquist plots recorded at 1.40 V vs. RHE in a 1.0 M KOH + 0.5 M urea electrolyte. (f) Chronopotentiometry response of Cu-NiOOH/Cu₂O/CM catalyst at 10 and 100 mA·cm⁻². The inset illustrates the three-electrode setup used for stability testing and the corresponding changes in UOR performance before and after the tests. (g) Comparison of UOR activity with recently reports (The blue bars denote the potential required to achieve a UOR current density of 10 mA·cm⁻², and the red bars denote the corresponding Tafel slope).

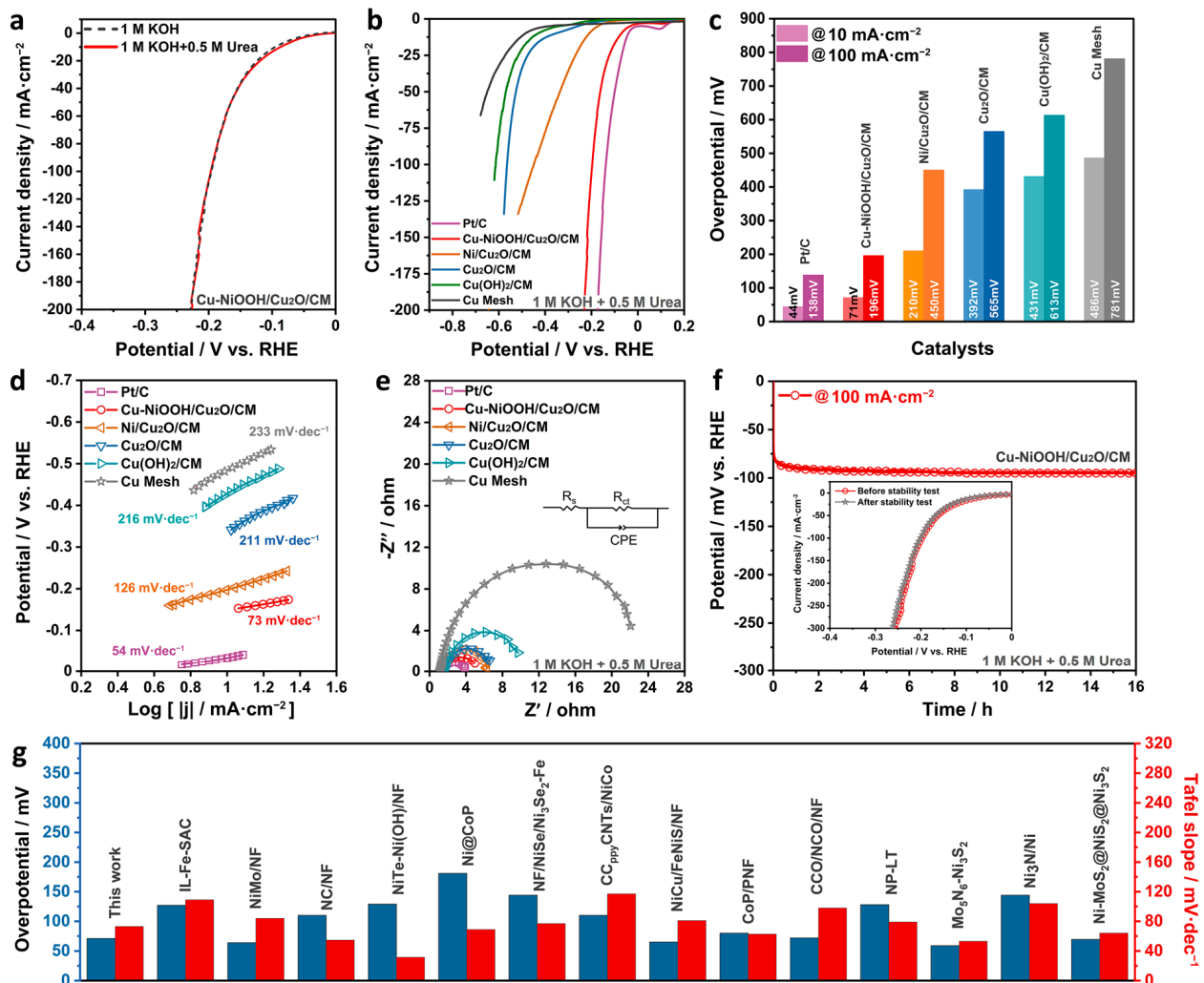


Figure 4. Electrochemical HER properties. (a) Polarization curves of Cu-NiOOH/Cu₂O/CM catalyst in a 1.0 M KOH electrolyte with and without 0.5 M urea. (b) Polarization curves of Pt/C, Cu-NiOOH/Cu₂O/CM, Ni/Cu₂O/CM, Cu₂O/CM, Cu(OH)₂/CM and pristine CM. (c) Summarized overpotential at the HER current density of 10 and 100 mA·cm⁻². (d) Tafel slopes. (e) Nyquist plots recorded at −0.20 V vs. RHE in a 1.0 M KOH + 0.5 M urea electrolyte. (f) Chronopotentiometry response of Cu-NiOOH/Cu₂O/CM catalyst at 10 mA·cm⁻². The inset illustrates the corresponding changes in HER performance before and after the tests. (g) Comparison of HER activity with recently reports (The blue bars denote the overpotential required to achieve a HER current density of 10 mA·cm⁻², and the red bars denote the corresponding Tafel slope).

It is noteworthy that relevant research has demonstrated that the insufficient and ineffective infiltration of the electrolyte into the electrode's surface and interior obstructs the full exposure of the catalyst's active sites, which negatively impacts the electrocatalytic UOR process. In addition, the accumulation of gas bubbles on the electrode surface during the catalytic reaction, if not released in time, leads to a pronounced 'bubble shielding effect', obstructing the mass transport of electrolyte ions [51–53]. In light of these considerations, contact angle tests were performed to assess the hydrophilic and aerophobic properties of the electrode surfaces, and the results are shown in Figures S12 and S13. As observed, the as-prepared Cu-NiOOH/Cu₂O/CM surface exhibits excellent hydrophilicity with a static contact angle (θ) of 15.7°, which is significantly smaller than that of Ni/Cu₂O/CM (141.7°), Cu₂O/CM (68.6°), and Cu(OH)₂/CM (168.6°), demonstrating that the surface's hydrophilicity, induced by electrochemical activation and featuring Cu-NiOOH dual active sites, can be effectively enhanced. Additionally, the electrochemical activation of Cu-

NiOOH/Cu₂O/CM significantly boosts its air bubble release capacity compared to the Ni/Cu₂O/CM precatalyst, enabling an air bubble to escape from its surface rapidly, within 200 ms. Therefore, it is reasonable to speculate that the bubbles generated on the Cu-NiOOH/Cu₂O/CM surface during the catalytic reaction can rapidly detach from the electrode surface, resulting in outstanding bifunctional UOR and HER performance.

Encouraged by the remarkable bifunctional UOR and HER activities of the Cu-NiOOH/Cu₂O/CM catalyst in a urea-containing alkaline electrolyte, a two-electrode electrolyzer was utilized, with the target Cu-NiOOH/Cu₂O/CM catalyst used as both the anode and cathode in a 1.0 M KOH + 0.5 M urea electrolyte. For the sake of comparison, overall water splitting was performed in a 1.0 M KOH solution, as evidenced by Figure 5a. As demonstrated by the LSV curves (derived from the reverse scan of the corresponding CV curves), the configuration of Cu-NiOOH/Cu₂O/CM || Cu-NiOOH/Cu₂O/CM required a cell voltage of 1.43 V vs. RHE to obtain a current density of 10 mA·cm⁻² for overall urea splitting, which is much lower than the potential needed for overall water splitting (1.62 V vs. RHE) and surpasses several efficient reported catalysts (as shown in Table 1). This demonstrates the promising application potential of the Cu-NiOOH/Cu₂O/CM electrode for urea oxidation-assisted hydrogen evolution [54]. Moreover, the chronopotentiometry measurement indicated the robust long-term stability of the Cu-NiOOH/Cu₂O/CM || Cu-NiOOH/Cu₂O/CM configuration at 30 mA·cm⁻². The morphological characterization of Cu-NiOOH/Cu₂O/CM revealed significant morphological changes during the long-term stability test (Figure S14), revealing that the material's superior UOR/HER catalytic activity is primarily maintained by the Cu-NiOOH dual active sites, with the macroscopic morphology of the sample having minimal influence on performance. XRD was also employed to evaluate the crystal structure of the Cu-NiOOH/Cu₂O/CM catalyst after stability testing. As shown in Figure S15, compared to Figure 2a, the target sample still predominantly consists of Cu₂O after long-term stability testing. However, new diffraction peaks appear at $2\theta = 35.3^\circ$, 38.5° , 48.7° , and 61.5° , corresponding to the crystal structure of CuO (JCPDS card No. 44-0706), indicating that an unavoidable and slight oxidation occurred during urea electrocatalysis. Furthermore, XPS was employed to characterize the surface valence state changes in the target sample on the anode side after stability testing. As illustrated in Figure S16, after prolonged urea electrocatalysis, the surface of the target material remains dominated by Ni and Cu. Compared to Figure 2c, more trivalent Ni³⁺ and divalent Cu²⁺ species are observed (consistent with the XRD results shown in Figure S15). These changes in valence states may be the reason for the performance degradation of the material after long-term stability testing.

Additionally, the Faradaic efficiency of the Cu-NiOOH/Cu₂O/CM catalyst was further evaluated through a water drainage strategy. The Faradaic efficiency of hydrogen evolution at the cathode catalyst during urea electrolysis is defined as the ratio of the H₂ amount produced during the catalytic process to the theoretically expected hydrogen amount [55]. Figure 5c demonstrates the collection of hydrogen produced during urea electrolysis while operating at a constant current density of 200 mA·cm⁻² using a 50 mL graduated cylinder, and the Faradaic efficiency for hydrogen generation was estimated to be approximately 100% (Figure 5d). The above suggests that this study is likely to pave the way for industrial green hydrogen production with lower energy consumption in the near future, and to simplify the fabrication of the self-supporting integrated transition metal electrode materials.

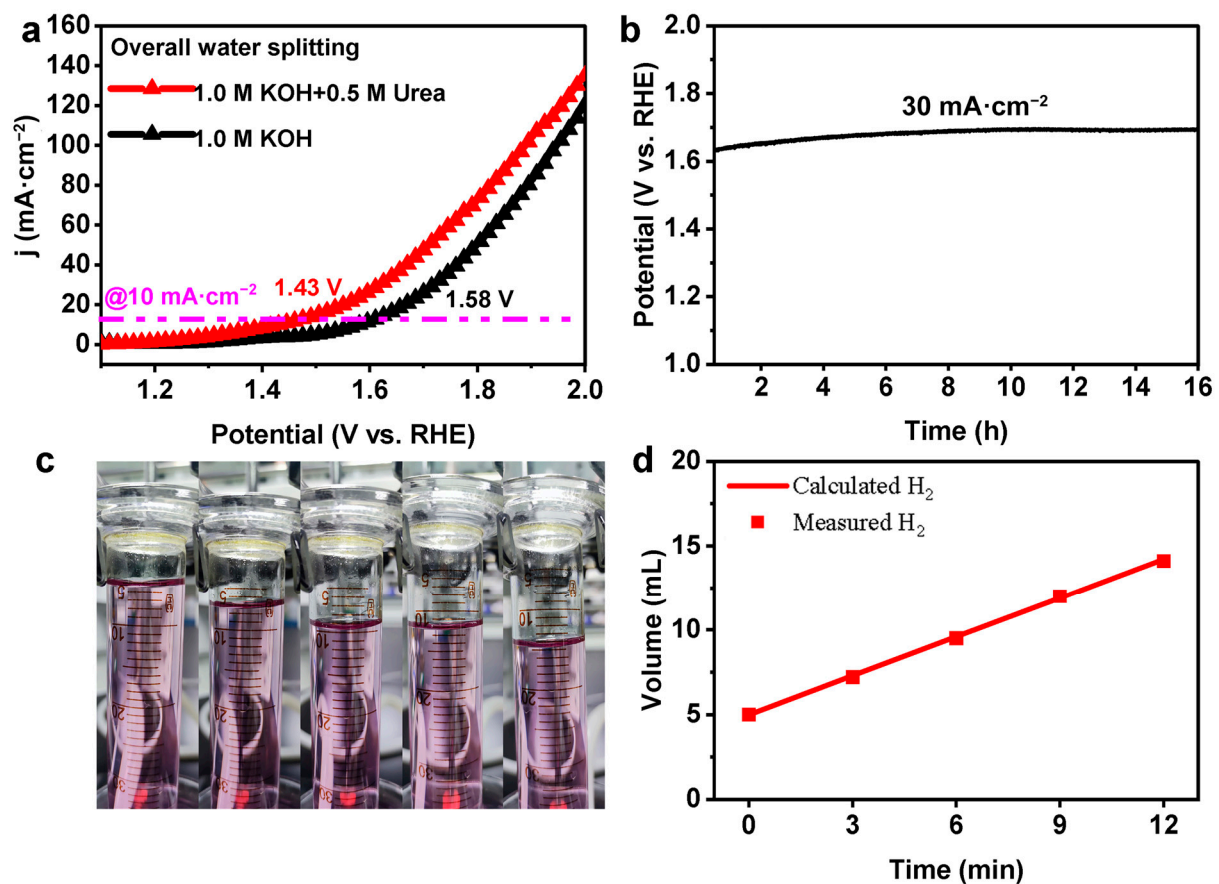


Figure 5. (a) Polarization curves of water electrolysis and urea electrolysis for Cu-NiOOH/Cu₂O/CM catalyst. (b) Urea electrolysis chronopotentiometry response recorded at 30 mA·cm⁻² for 16 h. (c) Enlarged digital images of the gas collection device of water splitting in a 1.0 M KOH + 0.5 M urea electrolyte and levels of hydrogen gas generated at 0, 180, 360, 540 and 720 s. (d) Faradaic efficiency of H₂ production in HER || UOR system upon operation time.

Table 1. Comparison of urea electrolysis of Cu-NiOOH/Cu₂O/CM with several reported catalysts.

Electrocatalyst	Urea Concentration in 1.0 M KOH Electrolyte	Cell Voltage at @10 mA cm ⁻²	Reference
Cu-NiOOH/Cu ₂ O/CM	0.5 M	1.43 V	This work
Ni/NiO@CrO _x	0.33 M	1.44 V	[56]
Ni/NiMoN	0.5 M	1.42 V	[57]
NiO/Ni ₂ P/NF	0.33 M	1.45 V	[58]
CoS _x /Ni(OH) ₂	0.5 M	1.48 V	[59]
Mo-NiS	0.5 M	1.51 V	[60]
NiFeSbP	0.5 M	1.54 V	[61]
Fe ₂ V-MOF	0.5 M	1.63 V	[62]

3. Experimental Section

3.1. Chemicals and Materials

Nickel sulfate hexahydrate (NiSO₄·6H₂O, ACS reagent, ≥98.0%), sodium sulfate (Na₂SO₄, BioXtra, ≥99.0%), boric acid (H₃BO₃, ACS reagent, ≥99.5%), hydrochloric (HCl, ACS reagent, 37%), potassium hydroxide (KOH, ACS reagent, ≥85.0%), ammonium peroxodisulfate ((NH₄)₂S₂O₈, ACS reagent, ≥98.0%), and sodium hydroxide (NaOH, ACS reagent, ≥97.0%) were purchased from Sigma-Aldrich (Shanghai, China). Absolute ethanol was obtained from Decon Labs, Lnc. (Shanghai, China). The IrO₂ and commercial Pt/C

(20 wt%) catalysts were purchased from Sigma-Aldrich (Shanghai, China). The Nafion perfluorinated resin solution (P400486, 5.0–5.4 wt%) was obtained from Aladdin Biochemical Technology Co., Ltd. (Shanghai, China). The copper mesh substrate was purchased from Sinopharm Chemical Reagent Co., Ltd. (Shanghai, China). No additional purification was made for the reagents, and all aqueous solutions were made with ultrapure deionized water (Milli-Q® Reference Pure Water System, Shanghai, China $\geq 18.2 \text{ M}\Omega @ 25^\circ\text{C}$).

3.2. Synthesis Methods

Preparation of Ni/Cu₂O/CM. The Cu mesh (CM) was cut into small pieces of $1.0 \times 1.5 \text{ cm}^2$, soaked in 2.0 M HCl solution, and ultrasonicated for 10 min to remove oxides from the electrode surface. The cleaned CM electrode was immersed in 30 mL of an aqueous solution containing 0.3 M (NH₄)₂S₂O₈ and 4.0 M NaOH, etched for 5 min to form Cu(OH)₂/CM, thoroughly rinsed with abundant quantities of deionized water, and subsequently air-dried at ambient temperature. Subsequently, the Cu(OH)₂/CM electrode was annealed at 450 °C for 2 h in 50 sccm of Ar gas to obtain the Cu₂O/CM electrode. Then, the Ni/Cu₂O/CM catalyst was prepared by electrodeposition. Using Cu₂O/CM as the cathode and a graphite rod as the anode, the electrolyte consisted of 0.5 M NiSO₄, 0.2 M Na₂SO₄, and 0.5 M H₃BO₃. Electrodeposition was performed at a current density of $50 \text{ mA}\cdot\text{cm}^{-2}$ for varying deposition times (120, 240, and 360 s). The resulting Ni/Cu₂O/CM electrodes were rinsed several times with deionized water and anhydrous ethanol, and air-dried for subsequent use. The morphological and color changes in the pristine CM, Cu(OH)₂/CM, Cu₂O/CM, and Cu-NiOOH/Cu₂O/CM electrodes are shown in Figure S1.

Preparation of Cu-NiOOH/Cu₂O/CM. To fabricate the Cu-NiOOH/Cu₂O/CM catalyst, the Ni/Cu₂O/CM catalyst was electrochemically activated using cyclic voltammetry (CV), which was conducted in a 1.0 M KOH electrolyte with a potential sweep range of 0–1.0 V (vs. SCE), a scan rate of $50 \text{ mV}\cdot\text{s}^{-1}$, and a total of 3 cycles. As shown in Figure S2, the electrochemically activated Cu-NiOOH/Cu₂O/CM catalyst delivered a significantly enhanced HER electrochemical activity.

Preparation of Pt/C and IrO₂ electrode. The Pt/C electrode was prepared by a drop-casting method. Specifically, 10 mg of commercial Pt/C (20 wt%) powder was dispersed in a solution containing 50 μL of Nafion solution and 950 μL of absolute ethanol. The mixed solution was ultrasonicated for 60 min to form a homogeneous catalyst ink. The black dispersion was then drop-cast onto the CM and left to dry in air overnight at room temperature for further measurements. The loading of Pt/C catalyst was $\sim 1.5 \text{ mg}\cdot\text{cm}^{-2}$. The IrO₂ electrode was also prepared by the abovementioned drop-casting method. The loading of IrO₂ catalyst was $\sim 1.5 \text{ mg}\cdot\text{cm}^{-2}$.

3.3. Physical Characterizations and Electrochemical Tests

For a detailed description of the physical characterizations and electrochemical tests covered in this paper, please refer to the ‘Supporting Information’.

4. Conclusions

In conclusion, we proposed an electrochemical activation method for the electrodeposited Ni/Cu₂O/CM heterostructured precatalyst, resulting in the Cu-NiOOH/Cu₂O/CM catalyst with accessible Cu-Ni^(III) dual active sites, high active surface area, good hydrophilic and aerophobic surface properties, and superior electrical conductivity. This catalyst demonstrated a remarkable electrocatalytic performance for UOR (1.32 and 1.38 V vs. RHE at 10 and $100 \text{ mA}\cdot\text{cm}^{-2}$) and HER (the overpotential of 71 mV at $10 \text{ mA}\cdot\text{cm}^{-2}$). The electrochemically activated NiOOH species exhibited exceptional bifunctional electrocatalytic activity for UOR/HER, benefiting greatly from the incorporation of Cu doping. The introduction of Cu accelerates the formation of trivalent Ni^(III), not only increasing the number of active NiOOH sites but also creating bifunctional active sites for UOR/HER. The urea-assisted electrolysis hydrogen production system showed a significantly decreased cell voltage of 1.43 V vs. RHE @ $10 \text{ mA}\cdot\text{cm}^{-2}$ in a 1.0 M KOH with 0.5 M urea, which

is about 190 mV lower than that of conventional water electrolysis. This approach of electrochemical activation is expected to be applicable to other Ni-based heterostructured nanomaterial systems, serving as a reference for further development of NiOOH catalysts with improved bifunctional UOR/HER catalytic properties.

Supplementary Materials: The following supporting information can be downloaded at: <https://www.mdpi.com/article/10.3390/catal14080496/s1>, Figure S1. Digital photographs illustrating the surface color variations of CM, Cu(OH)₂/CM, Cu₂O/CM, and Cu-NiOOH/Cu₂O/CM electrodes during the preparation process. Figure S2. Electrochemical activation. (a) Activation process, (b) HER performance comparison before and after activation. Figure S3. SEM images of Ni/Cu₂O/CM catalyst synthesized at various electrodeposition: (a) 120 s. (b) 240 s. (c) 360 s. Figure S4. SEM images of (a) CM, (b,c) Cu(OH)₂/CM and (d) Cu₂O/CM catalysts. Figure S5. XRD patterns of (a) Cu(OH)₂/CM and (b) Cu₂O/CM catalysts, indicating the successful transformation of the crystal structure. Figure S6. N₂ adsorption-desorption curves obtained from the BET analysis of the pristine CM, Cu(OH)₂/CM, Cu₂O/CM, Ni/Cu₂O/CM and Cu-NiOOH/Cu₂O/CM catalysts. Figure S7. The particle size distribution histogram of the electrodeposited Ni nanoparticles decorated on the surface of Cu₂O/CM. Figure S8. The magnified segment of the XRD patterns within the $2\theta = 40\text{--}45^\circ$ of Cu-NiOOH/Cu₂O/CM catalyst. Figure S9. XPS survey spectrum of the as-prepared Ni Mesh, Cu₂O/CM, Ni/Cu₂O/CM and Cu-NiOOH/Cu₂O/CM catalysts. Figure S10. Electrocatalytic OER properties. (a) Polarization curves of Cu-NiOOH/Cu₂O/CM, IrO₂, Cu₂O/CM, Cu(OH)₂/CM and pristine CM catalyst in a 1.0 M KOH electrolyte. (b) Tafel slopes. (c) Summarized overpotential at the OER current density of 10 and 50 mA·cm^{−2}. (d) Nyquist plots recorded at 1.60 V vs. RHE in a 1.0 M KOH electrolyte. (e) The plots of the current density versus the scan rate of Cu-NiOOH/Cu₂O/CM, Cu₂O/CM and Cu(OH)₂/CM catalysts. (f) Long-term chronopotentiometry response recorded at 50 mA·cm^{−2} for 16 h OER. Figure S11. Typical cyclic voltammograms curves within the non-Faraday potential range for UOR of Cu-NiOOH/Cu₂O/CM, Cu₂O/CM, Cu(OH)₂/CM catalyst at scan rate ranging from 20 to 120 mV·s^{−1}. Figure S12. Water contact angles on the as-prepared Cu(OH)₂/CM, Cu₂O/CM, Ni/Cu₂O/CM and Cu-NiOOH/Cu₂O/CM catalysts. Figure S13. Air contact angles on the Ni/Cu₂O/CM and Cu-NiOOH/Cu₂O/CM. Figure S14. SEM morphology before and after stability test of Cu-NiOOH/Cu₂O/CM catalyst. (a) before stability test, (b) after stability test. Figure S15. XRD pattern of Cu-NiOOH/Cu₂O/CM catalyst after stability test. Figure S16. High-resolution XPS of (a) Ni 2p and (b) Cu 2p in Cu-NiOOH/Cu₂O/CM catalyst after stability test. Table S1. Comparison of the UOR performance of Cu-NiOOH/Cu₂O/CM and other reported electrocatalysts in the past three years. Table S2. Comparison of the HER performance of Cu-NiOOH/Cu₂O/CM and other reported electrocatalysts in the past years. References [15,63–90] are cited in the supplementary materials.

Author Contributions: K.Z. and X.X. contributed equally to this work. K.Z. and Z.C. designed this work; K.Z., X.X., M.W., T.C., Q.J. and L.H. carried out the synthesis, characterization, and electrochemical experiments; K.Z., M.W. and Z.C. wrote the manuscript. The analysis of the experimental data, discussions of the results, and preparation of the manuscript were all carried out collaboratively by all authors. All authors have read and agreed to the published version of the manuscript.

Funding: This work was supported by the National Natural Science Foundation of China (No. 52201246), the Hainan Provincial Natural Science Foundation of China (No. 522QN280), the National Key Research and Development Program of China (No. 2022YFB3705703), and the Collaborative Innovation Center of Marine Science and Technology, Hainan University (XTCX2022HYC02).

Data Availability Statement: Data will be made available on request.

Conflicts of Interest: The authors declare no competing financial interests.

References

1. Sun, H.; Xu, X.; Fei, L.; Zhou, W.; Shao, Z. Electrochemical oxidation of small molecules for energy-saving hydrogen production. *Adv. Energy Mater.* **2024**, 2401242. [[CrossRef](#)]
2. Abdelghafar, F.; Xu, X.; Jiang, S.P.; Shao, Z. Designing single-atom catalysts toward improved alkaline hydrogen evolution reaction. *Mater. Rep. Energy* **2022**, 2, 100144. [[CrossRef](#)]
3. Guan, D.; Wang, B.; Zhang, J.; Shi, R.; Jiao, K.; Li, L.; Wang, Y.; Xie, B.; Zhang, Q.; Yu, J.; et al. Hydrogen society: From present to future. *Energy Environ. Sci.* **2023**, 16, 4926–4943. [[CrossRef](#)]

4. Fei, L.; Sun, H.; Ran, R.; Zhou, W.; Shao, Z. Self-supported nickel phosphide electrode for efficient alkaline water-to-hydrogen conversion via urea electrolysis. *Ind. Eng. Chem. Res.* **2021**, *60*, 1185–1193. [\[CrossRef\]](#)
5. Yu, J.; Li, Z.; Wang, C.; Xu, X.; Liu, T.; Chen, D.; Shao, Z.; Ni, M. Engineering advanced noble-metal-free electrocatalysts for energy-saving hydrogen production from alkaline water via urea electrolysis. *J. Colloid Interface Sci.* **2024**, *661*, 629–661. [\[CrossRef\]](#) [\[PubMed\]](#)
6. Ge, W.Y.; Lin, L.P.; Wang, S.Q.; Wang, Y.C.; Ma, X.W.; An, Q.; Zhao, L. Electrocatalytic urea oxidation: Advances in mechanistic insights, nanocatalyst design, and applications. *J. Mater. Chem. A* **2023**, *11*, 15100–15121. [\[CrossRef\]](#)
7. Li, Y.; Sun, Y.; Qin, Y.; Zhang, W.; Wang, L.; Luo, M.; Yang, H.; Guo, S. Recent advances on water-splitting electrocatalysis mediated by noble-metal-based nanostructured materials. *Adv. Energy Mater.* **2020**, *10*, 1903120. [\[CrossRef\]](#)
8. Chao, T.; Hu, Y.; Hong, X.; Li, Y. Design of noble metal electrocatalysts on an atomic level. *ChemElectroChem* **2019**, *6*, 289–303. [\[CrossRef\]](#)
9. Wang, K.; Wang, S.; Hui, K.S.; Gao, H.; Dinh, D.A.; Yuan, C.; Zha, C.; Shao, Z.; Tang, Z.; Hui, K.N. Synergistically boosting the elementary reactions over multiheterogeneous ordered macroporous Mo₂C/NC-Ru for highly efficient alkaline hydrogen evolution. *Carbon Energy* **2022**, *4*, 856–866. [\[CrossRef\]](#)
10. Wang, Z.L.; Liu, W.J.; Hu, Y.M.; Guan, M.L.; Xu, L.; Li, H.P.; Bao, J.; Li, H.M. Cr-doped CoFe layered double hydroxides: Highly efficient and robust bifunctional electrocatalyst for the oxidation of water and urea. *Appl. Catal. B-Environ.* **2020**, *272*, 118959. [\[CrossRef\]](#)
11. He, Y.T.; Yang, X.X.; Li, Y.S.; Liu, L.T.; Guo, S.W.; Shu, C.Y.; Liu, F.; Liu, Y.N.; Tan, Q.; Wu, G. Atomically dispersed Fe–Co dual metal sites as bifunctional oxygen electrocatalysts for rechargeable and flexible Zn–Air batteries. *ACS Catal.* **2022**, *12*, 1216–1227. [\[CrossRef\]](#)
12. Patil, S.J.; Chodankar, N.R.; Hwang, S.K.; Rama Raju, G.S.; Huh, Y.S.; Han, Y.K. Fluorine engineered self-supported ultrathin 2D nickel hydroxide nanosheets as highly robust and stable bifunctional electrocatalysts for oxygen evolution and urea oxidation reactions. *Small* **2022**, *18*, 2103326. [\[CrossRef\]](#) [\[PubMed\]](#)
13. Wang, J.M.; Zhao, Z.; Shen, C.; Liu, H.P.; Pang, X.Y.; Gao, M.Q.; Mu, J.; Cao, F.; Li, G.Q. Ni/NiO heterostructures encapsulated in oxygen-doped graphene as multifunctional electrocatalysts for the HER, UOR and HMF oxidation reaction. *Catal. Sci. Technol.* **2021**, *11*, 2480–2490. [\[CrossRef\]](#)
14. Liu, M.; Zou, W.; Qiu, S.; Su, N.; Cong, J.; Hou, L. Active site tailoring of Ni-based coordination polymers for high-efficiency dual-functional HER and UOR catalysis. *Adv. Funct. Mater.* **2024**, *34*, 2310155. [\[CrossRef\]](#)
15. Liu, G.Q.; Sun, Z.T.; Liu, D.M.; Li, Y.T.; Zhang, W.X. Enhancing the surface polarization effect via Ni/NiMoO_x heterojunction architecture for urea-assisted hydrogen generation. *J. Colloid Interface Sci.* **2023**, *629*, 1012–1020. [\[CrossRef\]](#)
16. Wan, K.; Luo, J.S.; Zhou, C.; Zhang, T.; Arbiol, J.; Lu, X.; Mao, B.W.; Zhang, X.; Fransaer, J. Hierarchical porous Ni₃S₄ with enriched high-valence Ni sites as a robust electrocatalyst for efficient oxygen evolution reaction. *Adv. Funct. Mater.* **2019**, *29*, 1900315. [\[CrossRef\]](#)
17. Sun, H.; Li, L.; Chen, Y.; Kim, H.; Xu, X.; Guan, D.; Hu, Z.; Zhang, L.; Shao, Z.; Jung, W. Boosting ethanol oxidation by NiOOH–CuO nano-heterostructure for energy-saving hydrogen production and biomass upgrading. *Appl. Catal. B-Environ.* **2023**, *325*, 122388. [\[CrossRef\]](#)
18. Xu, H.; Liao, Y.; Gao, Z.F.; Qing, Y.; Wu, Y.Q.; Xia, L.Y. A branch-like Mo-doped Ni₃S₂ nanoforest as a high-efficiency and durable catalyst for overall urea electrolysis. *J. Mater. Chem. A* **2021**, *9*, 3418–3426. [\[CrossRef\]](#)
19. Li, D.; Wan, W.J.; Wang, Z.W.; Wu, H.Y.; Wu, S.X.; Jiang, T.; Cai, G.X.; Jiang, C.Z.; Ren, F. Self-derivation and surface reconstruction of Fe-doped Ni₃S₂ electrode realizing high-efficient and stable overall water and urea electrolysis. *Adv. Energy Mater.* **2022**, *12*, 2201913. [\[CrossRef\]](#)
20. Wen, D.F.; Peng, W.D.; Zhang, W.T.; Xia, Y.; Ye, M.; Hu, W. Hetero-structured NiMoO₄/Ni₃S₄/MoS₂ pompons decorated nickel foam electrode for high-efficient urea and urine electrolysis. *Appl. Surf. Sci.* **2023**, *608*, 155166. [\[CrossRef\]](#)
21. Chai, H.M.; Ma, X.; Dang, Y.C.; Zhang, Y.Q.; Yue, F.; Pang, X.X.; Wang, G.Q.; Yang, C.M. Triple roles of Ni(OH)₂ promoting the electrocatalytic activity and stability of Ni₃S₄@Ni(OH)₂ in anion exchange membrane water electrolyzers. *J. Colloid Interface Sci.* **2024**, *654*, 66–75. [\[CrossRef\]](#) [\[PubMed\]](#)
22. Wang, Z.J.; Guo, P.; Liu, M.; Guo, C.; Liu, H.; Wei, S.X.; Zhang, J.; Lu, X. Rational design of metallic NiTe_x (x = 1 or 2) as bifunctional electrocatalysts for efficient urea conversion. *ACS Appl. Energy Mater.* **2019**, *2*, 3363–3372. [\[CrossRef\]](#)
23. Jin, C.L.; Hou, M.Y.; Li, X.; Liu, D.; Qu, D.; Dong, Y.L.; Xie, Z.Z.; Zhang, C.C. Rapid electrodeposition of Fe-doped nickel selenides on Ni foam as a bifunctional electrocatalyst for water splitting in alkaline solution. *J. Electroanal. Chem.* **2022**, *906*, 116014. [\[CrossRef\]](#)
24. Xu, X.C.; Liao, H.J.; Huang, L.; Chen, S.J.; Wang, R.; Wu, S.; Wu, Y.X.; Sun, Z.P.; Huang, H.T. Surface reconstruction and directed electron transport in NiSe₂/MoSe₂ Mott-Schottky heterojunction catalysts promote urea-assisted water splitting. *Appl. Catal. B-Environ.* **2024**, *341*, 123312. [\[CrossRef\]](#)
25. Jia, X.; Kang, H.J.; Yang, X.X.; Li, Y.L.; Cui, K.; Wu, X.H.; Qin, W.; Wu, G. Amorphous Ni(III)-based sulfides as bifunctional water and urea oxidation anode electrocatalysts for hydrogen generation from urea-containing water. *Appl. Catal. B-Environ.* **2022**, *312*, 121389. [\[CrossRef\]](#)
26. Tu, Z.T.; Liu, X.; Xiong, D.; Wang, J.Y.; Gong, S.Q.; Xu, C.; Wu, D.; Chen, Z.F. Ultrafast room-temperature activation of nickel foams as highly efficient electrocatalysts. *Chem. Eng. J.* **2023**, *475*, 146253. [\[CrossRef\]](#)

27. Yang, W.L.; Yang, X.P.; Hou, C.; Li, B.; Gao, H.T.; Lin, J.; Luo, X.L. Rapid room-temperature fabrication of ultrathin Ni(OH)₂ nanoflakes with abundant edge sites for efficient urea oxidation. *Appl. Catal. B-Environ.* **2019**, *259*, 118020. [\[CrossRef\]](#)
28. Zhang, N.; Wang, J.; Zhang, W.; Zhao, Y.; Dong, Z.; Wu, Z.; Xu, G.; Wang, L. Self-supported PdNi dendrite on Ni foam for improving monohydric alcohol and polyhydric alcohols electrooxidation. *Fuel* **2022**, *326*, 125083. [\[CrossRef\]](#)
29. Zhang, K.; Sun, P.; Huang, Y.; Tang, M.; Zou, X.; Pan, Z.; Huo, X.; Wu, J.; Lin, C.; Sun, Z.; et al. Electrochemical nitrate reduction to ammonia on CuCo nanowires at practical level. *Adv. Funct. Mater.* **2024**, 2405179. [\[CrossRef\]](#)
30. Wang, Q.X.; Cai, J.L.; Sun, Y.; Chen, W.Z.; Huang, H.; Wang, S.; Fu, L.; Xie, S. Urchin-like Au/Pd nanobranches for the oxygen reduction electrocatalysis. *ACS Appl. Nano Mater.* **2024**, *7*, 5534–5542. [\[CrossRef\]](#)
31. Zhang, J.; Zhou, F.; Huang, A.; Wang, Y.; Chu, W.; Luo, W. A copper interface promotes the transformation of nickel hydroxide into high-valent nickel for an efficient oxygen evolution reaction. *Inorg. Chem. Front.* **2023**, *10*, 5111–5116. [\[CrossRef\]](#)
32. Kim, B.K.; Kim, S.K.; Cho, S.K.; Kim, J.J. Enhanced catalytic activity of electrodeposited Ni-Cu-P toward oxygen evolution reaction. *Appl. Catal. B-Environ.* **2018**, *237*, 409–415. [\[CrossRef\]](#)
33. Li, X.L.; Ma, Y.J.; Yang, Z.; Xu, S.S.; Wei, L.M.; Huang, D.; Wang, T.; Hu, N.; Zhang, Y. Hierarchical heterostructures based on prickly Ni nanowires/Cu₂O nanoparticles with enhanced photocatalytic activity. *Dalton Trans.* **2016**, *45*, 7258–7266. [\[CrossRef\]](#) [\[PubMed\]](#)
34. Wei, C.; Liu, Y.; Liu, Q.; Xiang, W. Uniform and dense copper nanoparticles directly modified indium tin oxide electrode for non-enzymatic glucose sensing. *J. Electroanal. Chem.* **2019**, *835*, 273–280. [\[CrossRef\]](#)
35. Wang, X.X.; Li, L.; Wang, Z.; Tan, L.; Wu, Z.; Liu, Z.; Gai, S.; Yang, P. NiS₂/MoS₂ on carbon cloth as a bifunctional electrocatalyst for overall water splitting. *Electrochim. Acta* **2019**, *326*, 134983. [\[CrossRef\]](#)
36. Chen, L.; Zhang, X.; Jiang, W.; Zhang, Y.; Huang, L.; Chen, Y.; Yang, Y.; Li, L.; Hu, J. In situ transformation of Cu₂O@MnO₂ to Cu@Mn(OH)₂ nanosheet-on-nanowire arrays for efficient hydrogen evolution. *Nano Res.* **2018**, *11*, 1798–1809. [\[CrossRef\]](#)
37. Deng, Y.L.; Handoko, A.D.; Du, Y.H.; Xi, S.; Yeo, B.S. In situ Raman spectroscopy of copper and copper oxide surfaces during electrochemical oxygen evolution reaction: Identification of Cu^{III} oxides as catalytically active species. *ACS Catal.* **2016**, *6*, 2473–2481. [\[CrossRef\]](#)
38. Fedorov, A.V.; Kukushkin, R.G.; Yeletsky, P.M.; Bulavchenko, O.A.; Chesalov, Y.A.; Yakovlev, V.A. Temperature-programmed reduction of model CuO, NiO and mixed CuO–NiO catalysts with hydrogen. *J. Alloys Compd.* **2020**, *844*, 156135. [\[CrossRef\]](#)
39. Lu, Y.; Qin, Y.H.; Chen, M.Y.; Liu, G.F.; Qi, P.C.; Wu, H.; Tang, Y.W. Multi-dimensional Ni(OH)₂/(Ni(OH)₂(NiOOH)_{1.67})_{0.857}@Ni₃S₂ hierarchical structure for high-performance asymmetric supercapacitor. *Appl. Surf. Sci.* **2023**, *611*, 155625. [\[CrossRef\]](#)
40. Hu, Q.; Wang, Z.; Huang, X.; Qin, Y.; Yang, H.; Ren, X.; Zhang, Q.; Liu, J.; Shao, M.; He, C. Integrating well-controlled core-shell structures into “superaerophobic” electrodes for water oxidation at large current densities. *Appl. Catal. B-Environ.* **2021**, *286*, 119920. [\[CrossRef\]](#)
41. Li, L.; Zhang, L.C.; Gou, L.C.; Wei, S.C.; Hou, X.D.; Wu, L. High-performance methanol electrolysis towards energy-saving hydrogen production: Using Cu₂O-Cu decorated Ni₂P nanoarray as bifunctional monolithic catalyst. *Chem. Eng. J.* **2023**, *454*, 140292. [\[CrossRef\]](#)
42. Wang, H.; Ying, J.; Xiao, Y.X.; Chen, J.B.; Li, J.H.; He, Z.Z.; Yang, H.J.; Yang, X.Y. Ultrafast synthesis of Cu₂O octahedrons inlaid in Ni foam for efficient alkaline water/seawater electrolysis. *Electrochem. Commun.* **2022**, *134*, 107177. [\[CrossRef\]](#)
43. Luo, J.; Tang, L.; Song, J.; Zhou, J.; Liu, S.; Chang, T.; Fang, Y. Synergistic engineering of doped Ni₂P–Ni₁₂P₅ heterostructure electrocatalysts for urea oxidation reaction. *Mol. Catal.* **2024**, *564*, 114276. [\[CrossRef\]](#)
44. Liao, Y.; Chen, Y.Y.; Li, L.; Luo, S.; Qing, Y.; Tian, C.H.; Xu, H.; Zhang, J.X.; Wu, Y.Q. Ultrafine homologous Ni₂P–Co₂P heterostructures via space-confined topological transformation for superior urea electrolysis. *Adv. Funct. Mater.* **2023**, *33*, 2303300. [\[CrossRef\]](#)
45. Kim, M.J.; Min, K.; Ko, D.; Seong, H.; Eun Shim, S.; Baeck, S.H. Regulating the electronic structure of Ni₂P by one-step Co, N dual-doping for boosting electrocatalytic performance toward oxygen evolution reaction and urea oxidation reaction. *J. Colloid Interface Sci.* **2023**, *650*, 1851–1861. [\[CrossRef\]](#) [\[PubMed\]](#)
46. Zhao, G.; Rui, K.; Dou, S.X.; Sun, W. Boosting electrochemical water oxidation: The merits of heterostructured electrocatalysts. *J. Mater. Chem. A* **2020**, *8*, 6393–6405. [\[CrossRef\]](#)
47. Xu, S.; Ruan, X.; Ganesan, M.; Wu, J.; Ravi, S.K.; Cui, X. Transition metal-based catalysts for urea oxidation reaction (UOR): Catalyst design strategies, applications, and future perspectives. *Adv. Funct. Mater.* **2024**, *34*, 2313309. [\[CrossRef\]](#)
48. Wang, Y.L.; Yin, H.B.; Dong, F.; Zhao, X.G.; Qu, Y.K.; Wang, L.X.; Peng, Y.; Wang, D.S.; Fang, W.; Li, J.H. N-coordinated Cu–Ni dual-single-atom catalyst for highly selective electrocatalytic reduction of nitrate to ammonia. *Small* **2023**, *19*, 2207695. [\[CrossRef\]](#) [\[PubMed\]](#)
49. Xue, Y.; Zhao, J.; Huang, L.; Lu, Y.R.; Malek, A.; Gao, G.; Zhuang, Z.; Wang, D.; Yavuz, C.T.; Lu, X. Stabilizing ruthenium dioxide with cation-anchored sulfate for durable oxygen evolution in proton-exchange membrane water electrolyzers. *Nat. Commun.* **2023**, *14*, 8093. [\[CrossRef\]](#)
50. Du, W.; Feng, Y.; Jiang, J.; Zhao, T.; Xu, G.; Zhang, L. Preparation of hollow nanorod Co_xCu_{2–x}Se/CF electrode assembled from nanoparticles and its urea-assisted hydrogen production performance. *J. Alloys Compd.* **2024**, *970*, 172517. [\[CrossRef\]](#)
51. Xu, X.J.; Guo, T.; Xia, J.Y.; Zhao, B.L.; Su, G.; Wang, H.; Huang, M.; Toghan, A. Modulation of the crystalline/amorphous interface engineering on Ni–P–O-based catalysts for boosting urea electrolysis at large current densities. *Chem. Eng. J.* **2021**, *425*, 130514. [\[CrossRef\]](#)

52. Jiang, L.; Yang, N.; Yang, C.; Zhu, X.; Jiang, Y.; Shen, X.; Li, C.; Sun, Q. Surface wettability engineering: $\text{CoS}_x\text{-Ni}_3\text{S}_2$ nanoarray electrode for improving overall water splitting. *Appl. Catal. B-Environ.* **2020**, *269*, 118780. [\[CrossRef\]](#)
53. Xu, X.J.; Zhang, C.H.; Li, J.Y.; Liu, H.; Su, G.; Shi, Z.C.; Huang, M.H. Redistributing interfacial charge density of $\text{Ni}_{12}\text{P}_5/\text{Ni}_3\text{P}$ via Fe doping for ultrafast urea oxidation catalysis at large current densities. *Chem. Eng. J.* **2023**, *452*, 139362. [\[CrossRef\]](#)
54. Liu, M.Y.; Zou, W.H.; Cong, J.; Su, N.; Qiu, S.; Hou, L. Identifying and unveiling the role of multivalent metal states for bidirectional UOR and HER over Ni, Mo-trithiocyanuric based coordination polymer. *Small* **2023**, *19*, 2302698. [\[CrossRef\]](#) [\[PubMed\]](#)
55. Wang, M.; Zheng, X.; Li, Y.; Zou, Z.; Ling, Y.; Wang, Q. KCl-assisted rapid and low-cost synthesis of antiperovskite $(\text{Fe}_{1-x}\text{Cu}_x)_4\text{N}$ anchored on Cu_2O nanosheets for highly efficient electrochemical overall water splitting. *Chem. Eng. J.* **2023**, *460*, 141854. [\[CrossRef\]](#)
56. Xu, H.W.; Zhang, W.D.; Yao, Y.; Yang, J.; Liu, J.; Gu, Z.G.; Yan, X. Amorphous chromium oxide confined Ni/NiO nanoparticles-assembled nanosheets for highly efficient and stable overall urea splitting. *J. Colloid Interface Sci.* **2023**, *629*, 501–510. [\[CrossRef\]](#) [\[PubMed\]](#)
57. Fan, Y.Y.; Gu, Y.; Wang, D.; Jiao, Y.; Wu, A.; Tian, C. Hollow NiMo-based nitride heterojunction with super-hydrophilic/aerophobic surface for efficient urea-assisted hydrogen production. *J. Energy Chem.* **2024**, *95*, 428–439. [\[CrossRef\]](#)
58. Xu, X.; Ji, S.; Wang, H.; Wang, X.; Linkov, V.; Wang, R. Porous hetero-structured nickel oxide/nickel phosphide nanosheets as bifunctional electrocatalyst for hydrogen production via urea electrolysis. *J. Colloid Interface Sci.* **2022**, *615*, 163–172. [\[CrossRef\]](#) [\[PubMed\]](#)
59. Sang, B.; Xue, C.; Guo, S.; Wng, X.; Xie, S.; Wang, C.; Li, R.Q. A hierarchical $\text{CoS}_x/\text{Ni}(\text{OH})_2$ heterostructure as a bifunctional electrocatalyst for urea-assisted energy-efficient hydrogen production. *Chem. Commun.* **2024**, *60*, 6643–6646. [\[CrossRef\]](#)
60. Zhou, Y.; Wang, Y.; Kong, D.; Zhao, Q.; Zhao, L.; Zhang, J.; Chen, X.; Li, Y.; Xu, Y.; Meng, C. Revealing the reactant mediation role of low-valence Mo for accelerated urea-assisted water splitting. *Adv. Funct. Mater.* **2023**, *33*, 2210656. [\[CrossRef\]](#)
61. Shoostari Gugtaped, H.; Rezaei, M. Hierarchical flower-like NiFeSbP electrocatalyst toward efficient and stable urea-assisted electrolytic hydrogen production. *ACS Appl. Energy Mater.* **2022**, *5*, 15689–15700. [\[CrossRef\]](#)
62. Chai, N.; Kong, Y.; Jiang, Q.; Guo, Q.; Chen, T.; Ma, X.; Yi, F.Y. Vanadium-doped bimetallic nanoporous metal–organic frameworks as bifunctional electrocatalysts for urea-assisted hydrogen production. *ACS Appl. Nano Mater.* **2024**, *7*, 14392–14405. [\[CrossRef\]](#)
63. Du, H.; Hu, H.; Wang, X.; Ran, N.; Chen, W.; Zhu, H.; Zhou, Y.; Yang, M.; Wang, J.; Liu, J. Vertical cross-alignments of 2D semiconductors with steered internal electric field for urea electrooxidation via balancing intermediates adsorption. *Small* **2024**, 2401053. [\[CrossRef\]](#) [\[PubMed\]](#)
64. Chen, L.; Wang, L.; Ren, J.T.; Wang, H.Y.; Tian, W.W.; Sun, M.L.; Yuan, Z.Y. Artificial heterointerfaces with regulated charge distribution of Ni active sites for urea oxidation reaction. *Small Methods* **2024**, 2400108. [\[CrossRef\]](#) [\[PubMed\]](#)
65. Liu, C.; Li, F.; Xue, S.; Lin, H.; Sun, Y.; Cao, J.; Chen, S. Fe doped Ni_3S_2 nanosheet arrays for efficient and stable electrocatalytic overall urea splitting. *ACS Appl. Energy Mater.* **2022**, *5*, 1183–1192. [\[CrossRef\]](#)
66. Yuan, W.; Jiang, T.; Fang, X.; Fan, Y.; Qian, S.; Gao, Y.; Cheng, N.; Xue, H.; Tian, J. Interface engineering of S-doped $\text{Co}_2\text{P}@ \text{Ni}_2\text{P}$ core–shell heterostructures for efficient and energy-saving water splitting. *Chem. Eng. J.* **2022**, *439*, 135743. [\[CrossRef\]](#)
67. Liu, Z.; Zhang, C.; Liu, H.; Feng, L. Efficient synergism of NiSe_2 nanoparticle/ NiO nanosheet for energy-relevant water and urea electrocatalysis. *Appl. Catal. B-Environ.* **2020**, *276*, 119165. [\[CrossRef\]](#)
68. Kim, J.; Kim, M.C.; Han, S.S.; Cho, K. Accessible Ni-Fe-oxalate framework for electrochemical urea oxidation with radically enhanced kinetics. *Adv. Funct. Mater.* **2024**, *34*, 2315625. [\[CrossRef\]](#)
69. Chen, J.; Chen, H.; Yin, H.; He, H.; Wang, Z.; Yu, D.; Liang, J.; Huang, Y.; Qin, L.; Chen, D. Understanding the promotion mechanism of boron during the surface reconstruction of Ni_2B nanoflakes for efficient urea electrocatalytic oxidation. *Chem. Eng. J.* **2023**, *477*, 146885. [\[CrossRef\]](#)
70. Luo, F.; Pan, S.; Xie, Y.; Li, C.; Yu, Y.; Yang, Z. Atomically dispersed Ni electrocatalyst for superior urea-assisted water splitting. *J. Energy Chem.* **2024**, *90*, 1–6. [\[CrossRef\]](#)
71. Wu, T.H.; Liu, Y.S.; Hong, C.T.; Hou, B.W. Binary and nanostructured NiMn perovskite fluorides as efficient electrocatalysts for urea oxidation reaction. *J. Colloid Interface Sci.* **2024**, *653*, 1094–1102. [\[CrossRef\]](#) [\[PubMed\]](#)
72. Maheskumar, V.; Min, A.; Moon, C.J.; Senthil, R.A.; Choi, M.Y. Modulating the electronic structure of Ni/NiO nanocomposite with high-valence Mo doping for energy-saving hydrogen production via boosting urea oxidation kinetics. *Small Struct.* **2023**, *4*, 2300212. [\[CrossRef\]](#)
73. Zheng, Z.; Wu, D.; Chen, L.; Chen, S.; Wan, H.; Chen, G.; Zhang, N.; Liu, X.; Ma, R. Collaborative optimization of thermodynamic and kinetic for Ni-based hydroxides in electrocatalytic urea oxidation reaction. *Appl. Catal. B-Environ.* **2024**, *340*, 123214. [\[CrossRef\]](#)
74. Yang, L.; He, R.; Wang, X.; Yang, T.; Zhang, T.; Zuo, Y.; Lu, X.; Liang, Z.; Li, J.; Arbiol, J.; et al. Self-supported NiO/CuO electrodes to boost urea oxidation in direct urea fuel cells. *Nano Energy* **2023**, *115*, 108714. [\[CrossRef\]](#)
75. Jiang, H.; Bu, S.; Gao, Q.; Long, J.; Wang, P.; Lee, C.S.; Zhang, W. Ultrathin two-dimensional nickel-organic framework nanosheets for efficient electrocatalytic urea oxidation. *Mater. Today Energy* **2022**, *27*, 101024. [\[CrossRef\]](#)
76. Zhao, J.; Zhang, Y.; Guo, H.; Ren, J.; Zhang, H.; Wu, Y.; Song, R. Defect-rich $\text{Ni}(\text{OH})_2/\text{NiO}$ regulated by WO_3 as core–shell nanoarrays achieving energy-saving water-to-hydrogen conversion via urea electrolysis. *Chem. Eng. J.* **2022**, *433*, 134497. [\[CrossRef\]](#)

77. Sathyaseelan, A.; Elumalai, V.; Perumalsamy, M.; Ali, H.L.; Sajeev, A.; Kim, S.J. Toward highly accessible Fe-N₄ sites via rational design of metal chelated ionic liquids for ORR, OER and HER trifunctional electrocatalysis. *Chem. Eng. J.* **2024**, *489*, 151235. [\[CrossRef\]](#)
78. Yuan, F.H.; Mohammadi, M.R.; Ma, L.L.; Cui, Z.D.; Zhu, S.L.; Li, Z.Y.; Wu, S.L.; Jiang, H.; Liang, Y.Q. Electrodeposition of self-supported NiMo amorphous coating as an efficient and stable catalyst for hydrogen evolution reaction. *Rare Met.* **2022**, *41*, 2624–2632. [\[CrossRef\]](#)
79. Askari, N.; Tasviri, M.; Ghiasi, M.; Amiri, M.; Wark, M. One-pot synthesis of NiCe-LDH for efficient electrochemical water splitting: A comprehensive experimental and theoretical study. *Mater. Today Sustain.* **2024**, *26*, 100784. [\[CrossRef\]](#)
80. Li, Q.; Huang, N.; Zhu, W.; Ma, H.; Du, J.; He, X.; Wang, S.; Li, C.; Wang, W.; Weng, Y. Preparation of NiTe-Ni(OH)₂/NF active cathode material as an electrocatalyst for hydrogen evolution. *J. Alloys Compd.* **2024**, *990*, 174458. [\[CrossRef\]](#)
81. Abahussain, A.A.M.; Alharbi, A.F.; Wazeer, W.; El-Deeb, H.; Nassr, A.B.A.A. Stainless steel as gas evolving electrodes in water electrolysis: Boosting the electrocatalytic hydrogen evolution reaction on electrodeposited Ni@CoP modified stainless steel electrodes. *Fuel* **2024**, *368*, 131605. [\[CrossRef\]](#)
82. Deng, R.; Yao, H.; Wang, Y.; Wang, C.; Zhang, S.; Guo, S.; Li, Y.; Ma, S. Interface effect of Fe doped NiSe/Ni₃Se₂ heterojunction as highly efficient electrocatalysts for overall water splitting. *Chem. Eng. J.* **2024**, *488*, 150996. [\[CrossRef\]](#)
83. Qiu, Y.; Zhang, Y.; Yu, M.; Li, X.; Wang, Y.; Ma, Z.; Liu, S. Ni-Co-O-S derived catalysts on hierarchical N-doped carbon supports with strong interfacial interactions for improved hybrid water splitting performance. *Small* **2024**, *20*, 2310087. [\[CrossRef\]](#) [\[PubMed\]](#)
84. Zhang, Y.; Wu, D.; Yang, C.; Li, Y.; Yang, Z.; Xu, S.; Xiong, D.; Wang, L.; Chu, P.K. Reversible surface reconstruction of bifunctional NiCu/FeNi₂S₄ heterostructure catalyst for overall water splitting. *Int. J. Hydrogen Energy* **2024**, *62*, 418–428. [\[CrossRef\]](#)
85. Liao, Q.; You, T.; Liu, X.; Deng, K.; Liu, P.; Tian, W.; Ji, J. Coupled plasma etching and electrodeposition of CoP/NiO nanosheets with surface reconstruction for water-splitting. *J. Mater. Chem. A* **2024**, *12*, 9830–9840. [\[CrossRef\]](#)
86. Saranya, V.; Anandha, B.G.; Navaneethan, M.; Archana, J. Hierarchical CuCo₂O₄/NiCo₂O₄ on self-standing Ni foam for high-performance water electrolysis. *J. Alloys Compd.* **2024**, *988*, 173894. [\[CrossRef\]](#)
87. Jiang, X.; Kyriakou, V.; Song, C.; Wang, X.; Costil, S.; Deng, C.; Liu, T.; Jiang, T.; Liao, H. A novel multi-channel porous structure facilitating mass transport towards highly efficient alkaline water electrolysis. *J. Energy Chem.* **2024**, *93*, 511–518. [\[CrossRef\]](#)
88. Fang, B.; Jin, J.; Li, Y.; Dang, H.; Shao, M.; Zhao, L.; Yin, N.; Wang, W. Interfacial electronic modulation of Mo₅N₆/Ni₃S₂ heterojunction array boosts electrocatalytic alkaline overall water splitting. *Small* **2024**, *20*, 2310825. [\[CrossRef\]](#) [\[PubMed\]](#)
89. Xiong, L.; Qiu, Y.; Dong, H.; Gao, B.; Zhang, X.; Chu, P.K.; Peng, X. Metallic Ni₃N/Ni heterostructure for efficient hydrogen evolution reaction. *Int. J. Hydrogen Energy* **2024**, *59*, 400–407. [\[CrossRef\]](#)
90. Yu, H.; Pan, J.; Zhang, Y.; Wang, L.; Ji, H.; Xu, K.; Zhi, T.; Zhuang, Z. Designing multi-heterogeneous interfaces of Ni-MoS₂@NiS₂@Ni₃S₂ hybrid for hydrogen evolution. *Nano Res.* **2024**, *17*, 4782–4789. [\[CrossRef\]](#)

Disclaimer/Publisher's Note: The statements, opinions and data contained in all publications are solely those of the individual author(s) and contributor(s) and not of MDPI and/or the editor(s). MDPI and/or the editor(s) disclaim responsibility for any injury to people or property resulting from any ideas, methods, instructions or products referred to in the content.